



Modeling and Control of a Grid-Supporting Electrolyzer

MASTER OF SCIENCE THESIS

Mekonen Tesfamariam Gebreslasie

September 20, 2022

Masterthesis eingereicht im Rahmen der Masterprüfung
im Masterstudiengang Renewable Energy Systems
am Department Environmental Engineering
der Fakultät Life Sciences
der Hochschule für Angewandte Wissenschaften Hamburg

Betreuender Prüfer :Prof. Dr. Gerwald Lichtenberg (HAW-Hamburg)
Zweitgutachter : Dr. Georg Pangalos (Fraunhofer IWES)

Abgegeben am September 20, 2022



The work in this thesis was supported by Fraunhofer Institute for Wind Energy Systems IWES, Application Center for Integration of Local Energy Systems (ILES) together with Hamburg University of Applied Sciences. Their cooperation is hereby gratefully acknowledged.

Abstract

The transition of the fossil fuel based centralized power generation in many countries towards renewable resources based distributed generation enables to reduce greenhouse gas emission as well as energy sources dependency. Besides the positive aspects of increasing the share of renewables in the energy mix, the technical feasibility of integrating variable renewable sources should be considered. This thesis investigates electrolyzers as promising systems to compensate the stochastic and intermittent behavior of renewable sources by storing energy in the form of hydrogen. Moreover, the study mainly covers the potential of the electrolyzers to enhance the robustness and stability of the decentralized power systems which are decreased due to absence of rotating inertia. Thus, to balance generation and consumption, electrolyzers can play a crucial role. The current state of the art is to regard electrolyzers as loads and connect them to the grid mainly using transistor rectifiers.

In this thesis the interactions between an electrical grid, represented by a synchronous generator and an electrolyzer as a load are under investigation. Therefore, a model of synchronous generator, electrolyzer and power electronic devices for connection have been built, and a plausible parameterization is implemented. In a second step, the control algorithms for the power electronic devices are synthesized and analyzed regarding their grid supporting properties. Furthermore, a designated grid supporting control algorithm is adapted to ascertain the contribution of the electrolyzer in the frequency and voltage amplitude stability of the power network.

To study the impact of electrolyzers on power system stability, various Electromagnetic Transient (EMT) simulations have been performed. These simulations show that electrolyzers have a positive effect on frequency stability, as electrolyzers are able to respond for frequency deviations faster than conventional generator governors.

Table of Contents

Abstract	i
Acknowledgements	ix
1 Introduction	1
1-1 Problem Statement	2
1-2 Objectives	2
1-3 Thesis Outline	3
2 Theory Description and Modeling	5
2-1 Synchronous Generator	6
2-1-1 Synchronous Machine Theory	6
2-1-2 Mathematical Modeling	7
2-2 Power Converters	12
2-2-1 AC-DC Converter	12
2-2-2 DC-DC Converter	15
2-3 Electrochemical Model of PEM Electrolyzer	18
2-3-1 Water Electrolysis Technologies	19
2-3-2 V-I characteristics of PEM Electrolyzer	20
2-4 Balance of Plant of PEM Electrolyzer	25
3 Control Methodology	29
3-1 Control of the Synchronous Generator	29
3-1-1 Frequency Control	29
3-1-2 Voltage Amplitude Control	30
3-2 Control of Power Converters	31
3-2-1 Internal Model Control	31
3-2-2 Control of Rectifier	32
3-2-3 Control of Buck Converter	38
3-3 Power-to-Hydrogen Conversion	38

4	Model Application for Grid-Support	41
4-1	PEM Electrolyzer as FCR	43
4-2	PEM Electrolyzer for aFRR	47
4-3	Voltage Amplitude Regulation	47
5	Simulation Results and Discussions	49
5-1	Response to Step Changes	51
5-2	Response to Power System Disturbances	58
6	Conclusion	61
	Bibliography	63
	Glossary	69
	List of Acronyms	69
	List of Symbols	70
	An Appendix	73
-1	Electrolyzer model	73
-2	A MATLAB listing	73
-3	Controller parameters	74

List of Figures

1-1	Overview of applications based on water electrolysis process supplied by renewable energy sources: adapted from [1]	2
2-1	Electrolyzer system components	5
2-2	Schematic diagram of synchronous machine: adapted from [2]	7
2-3	Stator and rotor circuits of a synchronous machine: adapted from [3]	8
2-4	Block diagram of a synchronous generator equipped with a prime mover, governor and voltage excitation system:Extracted from [4]	12
2-5	Three-phase rectifier showing switches, input reactor and DC-link capacitor	14
2-6	Classic buck converter	16
2-7	Inductor Current in the CCM	16
2-8	3-leg interleaved buck converter	18
2-9	Schematics of PEM electrolyzer device	21
2-10	Polarization curve of PEM electrolyzer	22
2-11	Proposed electrolyzer stack model and grid interface	25
2-12	BoP of a PEM electrolyzer: blue-water management subsystem, red-hydrogen production subsystem, yellow-cooling subsystem. Extracted from [5]	27
2-13	Balance of plant load model	28
3-1	Simulink Blocks of a synchronous generator equipped with a prime mover, governor and voltage excitation system representation	30
3-2	General schematic diagram of IMC	31
3-3	Control block diagram of the Phase-Locked Loop (PLL)	32
3-4	Multivariable dynamic model of a VSC system	34
3-5	General block diagram of inner current control loop	34
3-6	Sinusoidal pulse width modulation	35
3-7	General block diagram of outer DC voltage control	37

3-8	Implementation of cascaded control structure in Simulink	38
3-9	Electrolyzer connection with power converters	40
4-1	Multiple time-frame frequency response in a power system following a frequency event: adapted from [6]	42
4-2	Power converter topologies for interfacing PEM electrolyzer with a power system	42
4-3	Structure of front end controller of PEM electrolyzer implemented in Simulink . .	44
4-4	Considered network topologies for grid-supporting electrolyzer study: Extracted from [7]	45
4-5	Frequency response of the system with different shares of electrolyser FCR capacity for a loss of 200 MW generation capacity: Extracted from [8]	46
4-6	Frequency response of the system with different shares of electrolyser FCR capacity for a loss of 200 MW load demand: Extracted from [8]	47
5-1	The electrolyzer model in Runtime module of Simulink	50
5-2	Response of the electrolyzer model to Voltage Source Converter (VSC) voltage set point increase	51
5-3	Response of the electrolyzer model to VSC voltage set point decrease	52
5-4	Response to the active power step up command	53
5-5	Response to the active power step down command	54
5-6	Simulation result to a step-up in grid voltage set point	56
5-7	Simulation result to a step-down in grid voltage set point	57
5-8	Response to a three-phase to ground fault	59
5-9	Response of the electrolyzer model to a load jump	60

List of Tables

2-1	Comparison of DC-DC Converter	18
2-2	Water Electrolysis Technologies Comparison	20
1	Parameters of the PEM electrolyzer model	73

Acknowledgements

My sincere gratitude goes to the Almighty God for sustaining me this far in pursuit of my life. In addition, I want to deeply thank my father for his indefinite support and motivation to have the base for this milestone.

No words could adequately express my gratitude to the government of Germany for providing me the right to pursue my education, as I was not only forbidden to study but also rejected to seek asylum in some other countries.

I would like to especially thank my university Supervisor Prof. Dr. Gerwald Lichtenberg for his close mentoring and assistance throughout the thesis. Many thanks to my Supervisor Dr. Georg Pangalos from Fraunhofer IWES for creating the opportunity to write my master thesis and continuous guidance.

Furthermore, I would like to express my gratitude to Mr. Carlos Cateriano Yanez for the constant support. His meticulous attitude to my work had certainly helped me to improve my final report. I'm also grateful to Mr. Christoph Kaufmann for the valuable inputs and suggestions for the thesis.

I have had the best experience working with the whole team at Fraunhofer IWES, in the application center for Integration of Local Energy Systems (ILES) Hamburg.

Hamburg,
September 20, 2022

Mekonen Tesfamariam Gebreslasie

Chapter 1

Introduction

The electric power generation in every nation continues to depend on fossil fuel such as coal, petroleum and natural gas. However, the concern of fossil fuel depletion in the future along with concerns over climate change and over national energy protection, when fossil fuel concentrations are limited to certain areas, has compelled the quest for renewable energy sources [9]. Renewable energy is generated from natural cycles that replenish themselves on a regular basis, such as wind, solar, geothermal and biomass. The European Commission aims to raise the share of renewable energy to be around 60% by the year 2050 in order to reduce emissions of polluting greenhouse gas by 85% to 95% compared to 1990 level of emissions [10].

Beside the positive aspects of increasing the share of renewables in the energy mix, the technical feasibility of integrating variable renewable sources should be considered. Due to the intermittent nature of these sources, they bring more fluctuations and uncertainty into the grid and complicate its operational management [9]. The difference between the varying electrical energy generation from renewable energy systems and consumption by loads leads to either an energy deficit or surplus in a grid. At present, these fluctuations are compensated by the conventional power plants. However, the conventional generators need to be decreased drastically to fulfill energy sector targets. Thus, Energy Storage Systems (ESS) are regarded as viable alternatives to compensate for the intermittent and distributed generators, so that the network demand can be met at all times [10].

Storage technologies with different characteristics have been developed to provide electrical storage for a wide range of power, i.e. pumped hydro, batteries, fly wheels and hydrogen technologies. According to the comparison among these storage systems in literature [11], the hydrogen storage system has a higher performance in terms of energy storage due to the highest energy density, flexibility and discharge time compared to the aforementioned storage systems. Thus, this study focuses mainly on the hydrogen technology to investigate its impact on the power network as well as its potential as a storage system.

Hydrogen is viewed as one of the most important drivers of the progressive decarbonization of the transportation, industrial and electricity sectors [1]. Principally, water electrolysis technology allows the exploitation of the surplus generation from renewable energy sources to produce green hydrogen. By carrying the energy in the form of molecules instead of electrons,

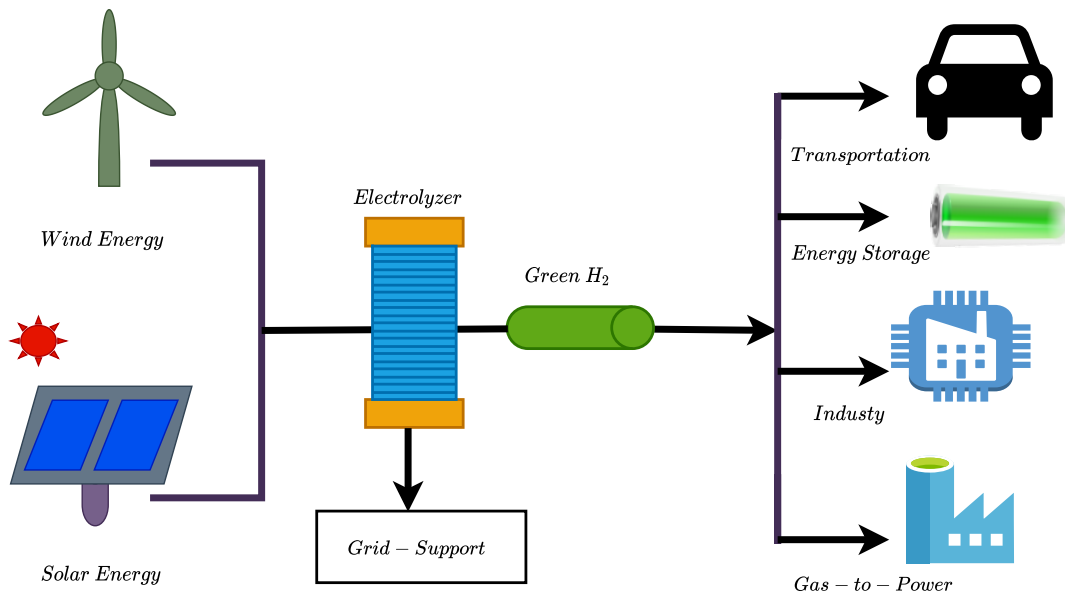


Figure 1-1: Overview of applications based on water electrolysis process supplied by renewable energy sources: adapted from [1]

long-term energy storage is enabled by hydrogen. Such stored energy allows supplying hydrogen fueling stations for fuel cell electric vehicles. Furthermore, hydrogen can be subjected to methanation in order to create synthetic gas that mainly used for electricity generation in gas turbines and for a handful of industrial processes. From all the cited applications shown in Figure 1-1, it is clear that the coupling of the electricity and gas sectors is worth studying and evaluating, especially in countries like Germany with a strong presence of chemical industrial activity and a large generation of electricity with gas fired power plants [12].

1-1 Problem Statement

The fossil fuel based centralized power system is directly connected to the grid, whereas the decentralized renewable energy based power generation is interfaced to the grid via power electronics. One of the major consequences of this transition towards a nearly 100% renewable system is the gradual loss of synchronous machines, their inertia, and control mechanisms. This loss of the rotational inertia changes the nature of the power system to a low-inertia network, resulting in critical power system stability challenges. Another challenge of distributed generators is their dependency on renewable energy sources which are characterized by having a stochastic and intermittent behavior.

1-2 Objectives

The aim of this thesis is to minimize the critical power system stability challenges in decentralized power systems by investigating the potential of a Proton Exchange Membrane (PEM)

electrolyzer for grid-support. First objective is to discover the importance of the faster response of the power electronic converters compared to conventional controllers for both active and reactive power support. The second objective is to model a PEM electrolyzer in order to study its impact in the power system network. The third objective is to identify proper control topology of power converters, that interface the PEM stack with the distribution or transmission network, to enhance the role of electrolyzer in ancillary services.

1-3 Thesis Outline

The study starts with a brief introduction in Chapter 1. Chapter 2 focuses on the theoretical description and mathematical derivation of all the system components needed for the study. In addition, the control design for a proper operation of the system is addressed in the third chapter. Chapter four deals with the model application in the frequency stability and voltage amplitude regulation of the grid. Furthermore, simulation results of the model are discussed in chapter five. Finally, chapter six concludes the thesis and provides hints of future work.

Theory Description and Modeling

Practical systems are necessarily to be described and represented mathematically, even if too difficult, in order to identify their characteristics so that to design proper control. The aim of this section is to explain the grid-supporting electrolyzer components shown in Figure 2-1 and derive their mathematical modelings to be implemented in MATLAB and Simulink. These mathematical expressions developed in this chapter are the basics for control design, modeling and simulation of the whole system. This chapter begins with explorations of a synchronous generator modeling for proper representation of a grid. After that, a derivation of the expression of a power converter is covered. Furthermore, the mathematical representation of an electrolyzer and its Balance of Plant (BoP) components are reviewed to investigate the load characteristics of the system.

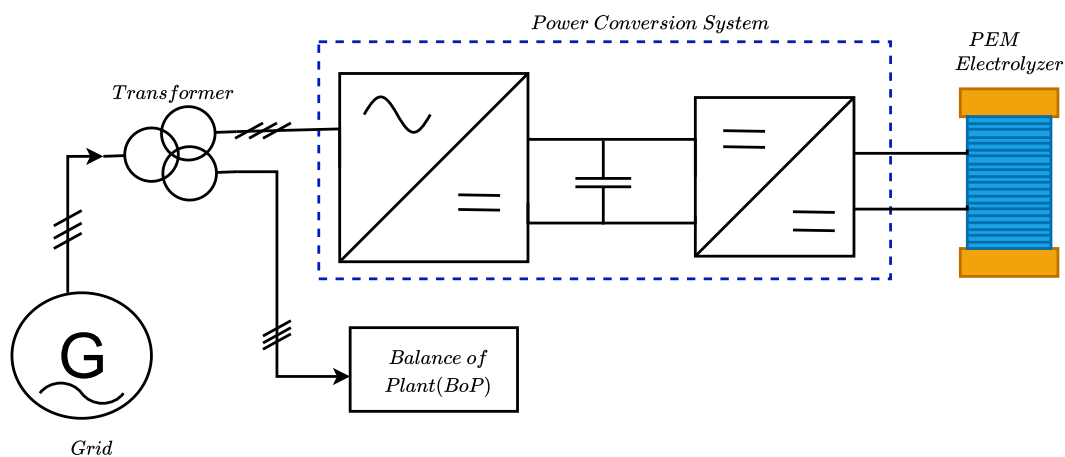


Figure 2-1: Electrolyzer system components

2-1 Synchronous Generator

The specific energy density of hydrogen is huge when it is compressed and transported at higher pressure and lower temperature. Therefore, to minimize the high delivery cost, the hydrogen production is preferred to be decentralized by being connected to the distribution or transmission network of the power system [13]. Such networks can be modeled as synchronous generators, as both of them have relatively similar operational characteristics. Therefore, the mathematical expression of the synchronous generator is derived here to represent the system network that supply electric power to the electrolyzer.

2-1-1 Synchronous Machine Theory

Synchronous generators form the principal source of electrical energy in power systems [3]. Every synchronous machine consists of two essential elements. The first part is the armature which is the stationary part that has three windings to carry three-phase induced voltage. And the second part is the rotor which is the rotating section that consists of a field winding which carries direct current to produce a magnetic field to induce alternating voltage in the armature windings and short-circuited damper windings that stabilize the electrical operation of the machine and provide start-up torque for the generator [2].

The schematic of the cross-section of a three-phase synchronous machine with one pair of field poles is shown in Figure 2-2. The rectangles with dots and x's indicate the three-phase windings a, b, and c. The current flow is assumed to be into the "x" and out of the "dot" located in the opposite side. The axes are determined based on the voltage polarity of the coils which are assumed to be plus to minus from the "x" to the "dot" [2]. An arbitrary δ is an angle between axis of phase a and q-axis.

When the rotor of the synchronous machine is moved by a prime-mover (e.g., a wind-turbine) and an excitation voltage is applied on the rotor-windings, a direct current is flowing in the field winding of the rotor which causes the creation of rotating magnetic field in the air-gap. Then, this magnetic field crosses the armature windings which enables a voltage induction in the stator.

When a load is connected to the stator, a three-phase current flows in the armature that produces another magnetic field in the air-gap which rotates at synchronous speed. The superposition of these two fields (created by rotor and stator windings) determines the machine's behavior in each operating point. According to [3], for a known armature current frequency f in Hz and pole pairs p of the machine, the synchronous speed n in rev/min can be determined as

$$n = \frac{60f}{p}. \quad (2-1)$$

The electromagnetic torque on the rotor acts in a direction to bring the magnetic fields into alignment. If the rotor field leads the armature field, the torque acts in opposition to the rotation with the machine acting as a generator. On the other hand, if the rotor field lags the stator field, the torque acts in the direction of rotation with the machine acting as a motor. In other words, for generator action, the rotor field leads the armature field by the forward torque of a prime mover; for motor action, the rotor field lags behind the armature field due to the retarding torque of shaft load [14].

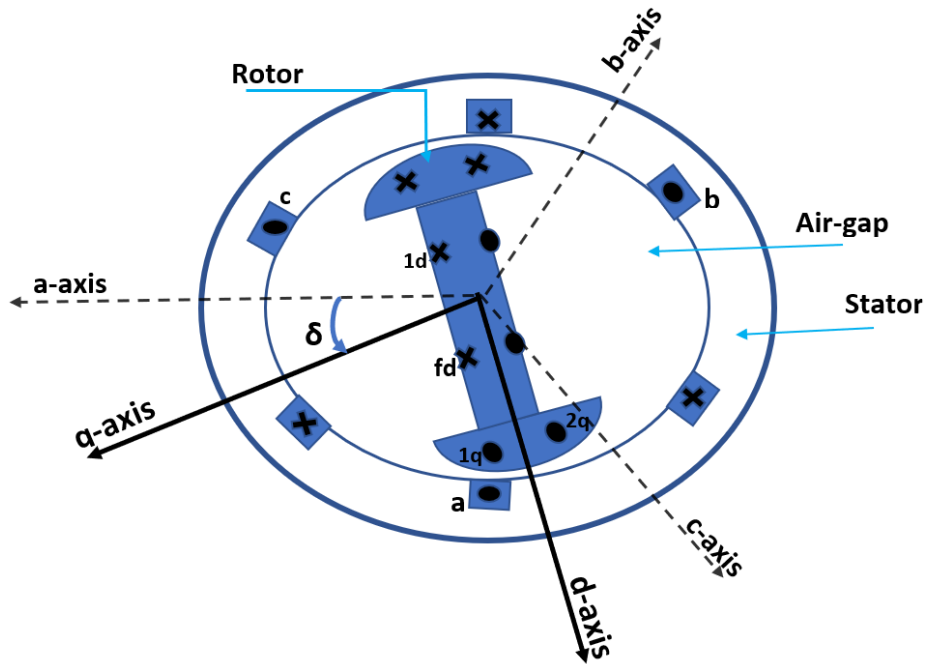


Figure 2-2: Schematic diagram of synchronous machine: adapted from [2]

There are two basic rotor structures, which are non-salient and salient poles, depending on their speed.

Non-salient poles: have round rotors with uniform air-gap that operate at high speeds. They have less number of poles and are used mainly in steam and gas turbines.

Salient poles: have rotors with projecting poles that have often short-circuited damper windings and circumferentially variable air-gap. They rotate at low speed and consist of higher number of poles to produce the rated frequency. Such rotors are mainly applied in hydraulic and wind turbines.

In this thesis salient pole with one pole pair and three damper windings is considered to drive the mathematical modeling of the machine.

2-1-2 Mathematical Modeling

The cross-section of the synchronous generator shown in Figure 2-2 can be simplified to a circuit diagram in order to determine its mathematical expression as demonstrated in Figure 2-3. Where a , b and c denote stator phase windings, fd and kd indicate d-axis field windings and damper circuit respectively, whereas kf is q-axis damper circuit, $k = 1, 2, \dots, n$; n denotes no. of damper circuits and ω_r is rotor angular velocity electrical in rad/s [15]. According to [2], in developing equations of synchronous generator, the following assumptions are made:

- the stator windings are sinusoidally distributed along the air-gap as far as the mutual effects with rotor are concerned,

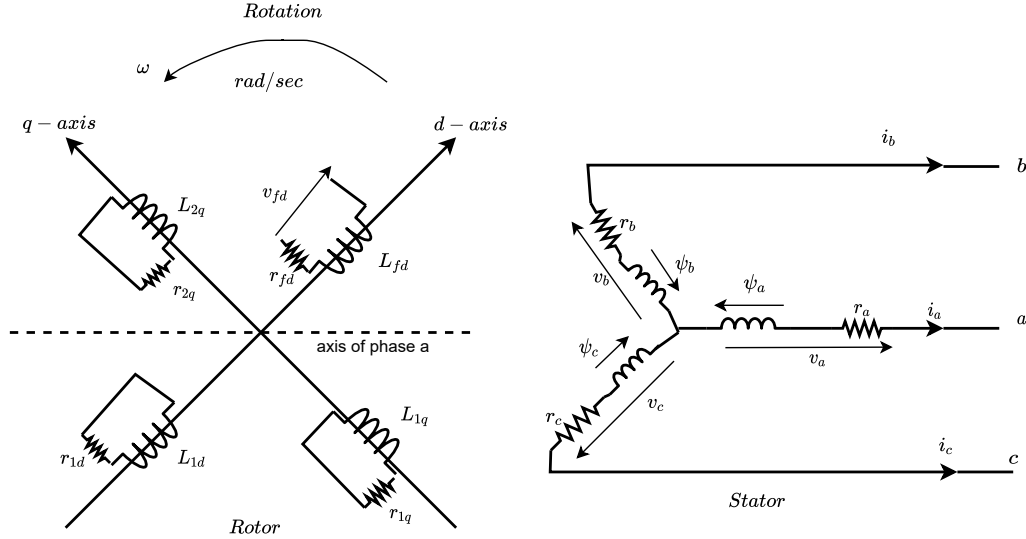


Figure 2-3: Stator and rotor circuits of a synchronous machine: adapted from [3]

- the stator slots cause no appreciable variation of the rotor inductances with rotor position,
- magnetic hysteresis is negligible,
- magnetic saturation effects are negligible.

Applying the fundamental Kirchhoff's and Faraday's laws, the system is expressed by three voltage equations of the stator windings and four voltage equations of rotor windings that consist of one field winding and three amortisseur (or damper) windings equations as follows

$$\mathbf{v} = \mathbf{r} \cdot \mathbf{i} + \frac{d\psi}{dt} \quad (2-2)$$

where

$$\begin{aligned} \mathbf{v} &= [v_a \ v_b \ v_c \ v_{fd} \ v_{1d} \ v_{1q} \ v_{2q}]^T, \\ \mathbf{r} &= [r_a \ r_b \ r_c \ r_{fd} \ r_{1d} \ r_{1q} \ r_{2q}]^T, \\ \mathbf{i} &= [i_a \ i_b \ i_c \ i_{fd} \ i_{1d} \ i_{1q} \ i_{2q}]^T, \\ \psi &= [\psi_a \ \psi_b \ \psi_c \ \psi_{fd} \ \psi_{1d} \ \psi_{1q} \ \psi_{2q}]^T. \end{aligned}$$

In addition, applying Newton's law, the system consists of two mechanical equations that include speed of shaft and swing equation [16], expressed as:

$$\frac{d\theta_{shaft}}{dt} = \frac{2}{P}\omega. \quad (2-3)$$

$$J\frac{2}{P}\frac{d\omega}{dt} = T_m - T_e - T_{fw}. \quad (2-3a)$$

$$\begin{aligned} T_e &= \frac{P_e}{\omega_s} \\ &= \frac{v_a i_a + v_b i_b + v_c i_c}{\omega_s}. \end{aligned} \quad (2-3b)$$

Where ψ is flux linkage, r is winding resistance, J is the inertia constant, P is the number of magnetic poles per phase, T_m is the mechanical torque applied to the shaft, T_e is the electrical torque and T_{fw} is a friction windage torque [17].

The flux linkage is related to current by

$$\psi = \mathbf{L}\mathbf{i}. \quad (2-4)$$

Where L is the machine inductance matrix, which is a function of the rotor position and the saturation condition of the machine.

The differential equation to be solved can be expressed in terms of winding flux from Eq. (2-2) and Eq. (2-4) as

$$\frac{d}{dt}[\psi] = \mathbf{v} - \mathbf{r}\mathbf{L}^{-1}[\psi] \quad (2-5)$$

The basic differential equation (2-3) can be used for simulation[17]. However, the variable flux linkage of stator and rotor windings associated with the stationary abc frame are time-varying, which causes problems to feedback control. In addition, the interaction between the three phases represents another drawback [3].

To solve these problems, R. H. Park in the 1920s proposed a rotating reference frame theory for electrical machine analysis [18]. By transforming the model from the stationary frame of reference to the synchronously rotating frame of reference, the positive-sequence components at fundamental frequency become constants and the interaction between the phases is avoided [19]. Park's transformation consists of two main axes: a direct axis d centered magnetically in the center of the north pole and a quadrature axis q selected arbitrary as leading or lagging the d-axis by 90 degree [3]. The arbitrary location and direction of both axes are indicated in Figure 2-2 and Figure 2-3.

The Park's transformation for electrical engineers can be formulated as:

$$T_{abc/dq0} = \sqrt{\frac{2}{3}} \begin{bmatrix} \cos \theta & \cos(\theta - \frac{2\pi}{3}) & \cos(\theta + \frac{2\pi}{3}) \\ \sin \theta & -\sin(\theta - \frac{2\pi}{3}) & -\sin(\theta + \frac{2\pi}{3}) \\ \frac{1}{\sqrt{2}} & \frac{1}{\sqrt{2}} & \frac{1}{\sqrt{2}} \end{bmatrix} \quad (2-6)$$

where θ is the electrical angle of a grid voltage. In the formula, there exist a third axis 0 for power flow during unbalanced operation of the system [3]. Then the transformed voltage is given by

$$\begin{bmatrix} e_d \\ e_q \\ e_0 \end{bmatrix} = T_{abc/dq0} \begin{bmatrix} v_a \\ v_b \\ v_c \end{bmatrix} \quad (2-7)$$

In addition, being an orthogonal matrix, the inverse Park's transformation can be obtained as:

$$T_{dq0/abc} = (T_{abc/dq0})^{-1} = (T_{abc/dq0})^T \quad (2-8)$$

Applying (2-6) in (2-2), the rotor voltage equations remain the same in both stationary abc frame and dq0 rotating frame of reference, as the rotor moves at synchronous speed in such machines [2]. Whereas the armature voltage formula is modified to

$$e_d = i_d r_a - \omega \psi_q + \frac{d\psi_d}{dt} \quad (2-9)$$

$$e_q = i_q r_a + \omega \psi_d + \frac{d\psi_q}{dt} \quad (2-9a)$$

$$e_0 = i_0 r_a + \frac{d\psi_0}{dt} \quad (2-9b)$$

Due to the relative motion between the stationary stator windings and the synchronously rotating magnetic field, Electromotive Force (EMF) is induced in the armature winding. Therefore, to consider the effect of the relative motion, the terms $-\omega \psi_q$ and $\omega \psi_d$ are added to the voltage equations in d-axis and q-axis of armature windings respectively [2].

In power system analysis, it is usually convenient to use a per-unit system to normalize system variables. Compared to the use of physical units (amperes, volts, ohms, webers, henrys etc.), the per-unit system offers computational simplicity by eliminating units and expressing system quantities as dimensionless ratios [3]. Thus,

$$\text{quantity in per unit} = \frac{\text{actual quantity}}{\text{base value of quantity}}. \quad (2-10)$$

Therefore, throughout this thesis, all values used in the simulation are in per unit.

The transient stability of such synchronous generator is determined by 9th order dynamic model that include three due to stator, four due to rotor and two due to swing equations.

The stator differential equations in per unit can be rewritten as :

$$\frac{1}{\omega_0} \frac{d\psi_d}{dt} = r_a i_d + (1 + \Delta\omega) \psi_q + v_d \quad (2-11)$$

$$\frac{1}{\omega_0} \frac{d\psi_q}{dt} = r_a i_q - (1 + \Delta\omega) \psi_d + v_q \quad (2-11a)$$

$$\frac{1}{\omega_0} \frac{d\psi_0}{dt} = r_a i_0 + v_0 \quad (2-11b)$$

These have a time constant that is

$$\frac{1}{\omega_0} = \frac{1}{2\pi i * 50} = 0.0032 \quad (2-11c)$$

This is about 1/6th of a cycle and is much faster than the phenomena that transient stability is concerned with [2]. Then the differential equations become normal algebraic equations. Furthermore, the effect of considering stator transients on speed deviation and rotor angle swings is quite negligible [3]. As a result, Stator transients are not usually considered in transient stability studies. Therefore, the 9th order of dynamic equations of the synchronous machine is reduced to 6th order of dynamic model that includes only rotor and swing dynamic equations which is to be implemented in this thesis.

The internal machine dynamics are thus characterized by the transients in the rotor circuits. The following derivation of this section is taken from work done in [4]. Rotor dynamics originate in the armature reaction, i.e., in the effect of the stator field on the rotor currents, which can be described through flux linkage dynamics

$$\dot{\Psi}_{d,f} = \frac{\omega_0 r_f}{x_{d,a,u}} v_f^d - \frac{\omega_0 r_f}{x_f} (\Psi_f^d - \Psi_{d,a}) \quad (2-12)$$

$$\dot{\Psi}_{D1} = -\frac{\omega_0 r_{D1}}{x_{D1}} (\Psi_{D1} - \Psi_{d,a}) \quad (2-12a)$$

$$\dot{\Psi}_{Q1} = -\frac{\omega_0 r_{Q1}}{x_{Q1}} (\Psi_{Q1} - \Psi_{q,a}) \quad (2-12b)$$

$$\dot{\Psi}_{Q2} = -\frac{\omega_0 r_{Q2}}{x_{Q2}} (\Psi_{Q2} - \Psi_{q,a}) \quad (2-12c)$$

Here, subscripts f , $D1$, $Q1$, and $Q2$ stand for the quantities of the field circuit, d-axis damping circuit and two q-axis damping circuits respectively, whereas Ψ , r , and x denote the respective flux linkage, resistance and reactance of a circuit; v_f is the exciter output voltage, ω_0 designates the synchronous angular velocity, and $x_{d,a,u}$ stands for the unsaturated mutual reactance. The armature flux linkages are expressed as follows:

$$\Psi_{d,a} = \hat{x}_{d,a,s} (-i_{d,s} + \frac{\Psi_{d,f}}{x_f} + \frac{\Psi_{D1}}{x_{D1}}) \quad (2-12d)$$

$$\Psi_{q,a} = \hat{x}_{q,a,s} (-i_{q,s} + \frac{\Psi_{Q1}}{x_{Q1}} + \frac{\Psi_{Q2}}{x_{Q2}}) \quad (2-12e)$$

with the sub-transient, saturated, mutual reactance $\hat{x}_{d,a,s}$ and $\hat{x}_{q,a,s}$ defined in the form:

$$\hat{x}_{d,a,s} = \left(\frac{1}{x_{d,a,s}} + \frac{1}{x_f} + \frac{1}{x_{D1}} \right)^{-1} \quad (2-12f)$$

$$\hat{x}_{q,a,s} = \left(\frac{1}{x_{q,a,s}} + \frac{1}{x_{Q1}} + \frac{1}{x_{Q2}} \right)^{-1} \quad (2-12g)$$

Finally, the inclusion of stator circuit balance completes the set of algebraic equations in (2-5) describing the internal generator dynamics:

$$e_{d,s} = -r_a i_{d,s} + x_l i_{q,s} - \Psi_{q,a} \quad (2-12h)$$

$$e_{q,s} = -r_a i_{q,s} + x_l i_{d,s} - \Psi_{d,a} \quad (2-12i)$$

Stator voltages and currents are denoted by $e_{dq,s}$ and $i_{dq,s}$, while r_a and x_l represent the armature resistance and leakage reactance respectively. Combining (2-3) and (2-12) with the 6 controller states depicted in Figure 2-4 yields a 12th order model [4].

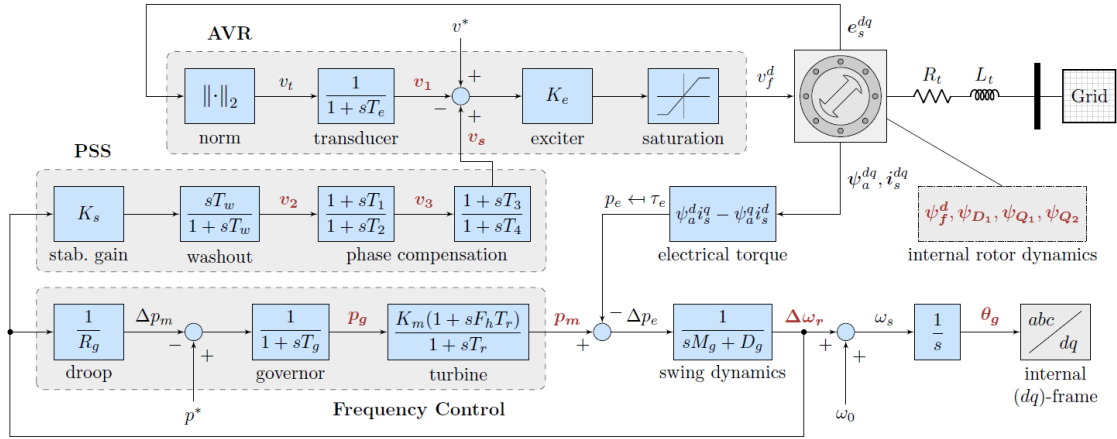


Figure 2-4: Block diagram of a synchronous generator equipped with a prime mover, governor and voltage excitation system: Extracted from [4]

2-2 Power Converters

The main load considered in this thesis is the hydrogen producer electrolyzer which needs DC power. Therefore, a power conversion system is implemented to connect the electrolyzer with the AC grid. The electrical system that converts AC voltage to DC voltage is called a rectifier. Usually, the electrolyzer is connected to the rectifier via a DC-DC converter for proper operation and secure lifespan. Most of electrolyzers operate at a low voltage compared to the output of rectifier or DC bus. Therefore, the DC-DC converter specially buck converter steps down the voltage to the operating range of the electrolyzer. Another reason is the DC-DC converters can be configured in different ways to increase the input current for a constant input voltage so that to enhance the hydrogen production. In addition, the lifespan of electrolyzers can be improved by decreasing the ripple effect using a high switching frequency of DC-DC converter. Thus, both the rectifier and DC-DC power converters are described and modeled in this section.

2-2-1 AC-DC Converter

Many types of AC-DC converters can be used to supply power depending on their electrical requirements based on their application. According to [20], it is noted that the requested stack voltage can vary from a few to hundreds of volt; whereas the current is included between 10 to thousands of amps, depending strongly on the rated power of the electrolyzer (i.e., from watt to megawatt range). In order to choose the right rectifier topology for a given electrolyzer application, different requirements and specifications must be taken into consideration [1]. One of them is to provide precise DC current control to manage the hydrogen flow rate and energy efficiency of the electrolyzer. Another consideration is to meet the international standards and requirements such as IEEE 519-2014 regarding input current harmonics injected in the AC power supply. In addition, the system should have high reliability to ensure a continuity of service in case of electrical failures and low cost to reduce the global cost. Finally, electrolyzer must be kept at small low- and high-frequency current ripple to extend its life span while optimizing the specific energy consumption.

A three-phase rectifier that consists of six switches is applicable for high power application by converting three-phase AC voltage to DC voltage. Depending on their application, the switches can be diodes, thyristors or transistors (e.g., IGBT, MOSFET etc.) [21]. The rectifier with diode switches can deliver only a constant output voltage given by

$$V_{dc} = 3\sqrt{6} \frac{V_{rms}}{\Pi}, \quad (2-13)$$

where V_{rms} is the line-to-line root-mean-square voltage of the grid in V. In addition, such rectifier deliver current to supply the electrolyzer in which the DC output power depends on the electrical features of the AC power supply and the electrolyzer as well. If the AC power supply was based on a wind turbine conversion system, the output voltage of the rectifier would fluctuate according to the wind speed. For this reason, uncontrolled diode-based rectifiers are not directly coupled with an electrolyzer system.

Compared to the rectifier based on diodes, thyristor-based rectifier allows delivering a controlled current, which is carried out through their firing angle, so that to manage the hydrogen flow rate and energy efficiency of the electrolyzer when coupling with renewable energy sources [1]. The output DC voltage of such rectifier with a firing angle α is determined by

$$V_{dc} = 3\sqrt{6} \frac{V_{rms}}{\Pi} \cos\alpha. \quad (2-14)$$

However, in controlling the rectifier through firing angle, it leads to the increase of current harmonic content and a decrease of the power factor due to the generation of a reactive power [22].

Again considering the comparison between the thyristor and transistor based rectifier, by the use of Integrated Gate Bipolar Transistors (IGBT) instead of thyristors in power converters, harmonics are mitigated, and their impact is lessened since the higher switching frequency of the power devices can be increased, and consequently, the frequency of harmonics is increased too. It makes their suppression easier and minimizes the effect on the electrolyzers [1]. Therefore, the three-phase rectifier topology implemented in this thesis is based on IGBT switches where their gate is triggered by Pulse Width Modulation (PWM) which gives high flexibility by providing freedom of output control. Such converter is also called Voltage Source Converter (VSC) or Active Front End (AFE) that converts electrical energy from AC to DC voltage or from DC to AC voltage according to an input three-phase modulation wave. However, in this case, it is designed to transfer power in one direction from AC to DC to supply the electrolyzer.

The label of the VSC as shown in Figure 2-5 consists of three-phase AC voltage V_a , V_b and V_c of grid, resistor R (representing internal resistances of line inductors and switches when turn on) and inductor L of line-impedance, line currents i_a , i_b and i_c , six IGBT switches denoted by S_i ($i = 1..6$), DC-link capacitor C and output DC voltage V_{dc} . The architecture of the converter indicates each emitter of the IGBT switch is connected to each phase in order to transfer power from AC grid to DC load.

The converter topology can be considered like a two voltage source (i.e., grid voltage and output DC voltage) linked by input reactor [19]. Applying Kirchhoff's voltage law, for sources and line elements of phase a, yields

$$V_a = Ri_a + L \frac{di_a}{dt} + \frac{V_{dc}}{2} d_a. \quad (2-15)$$

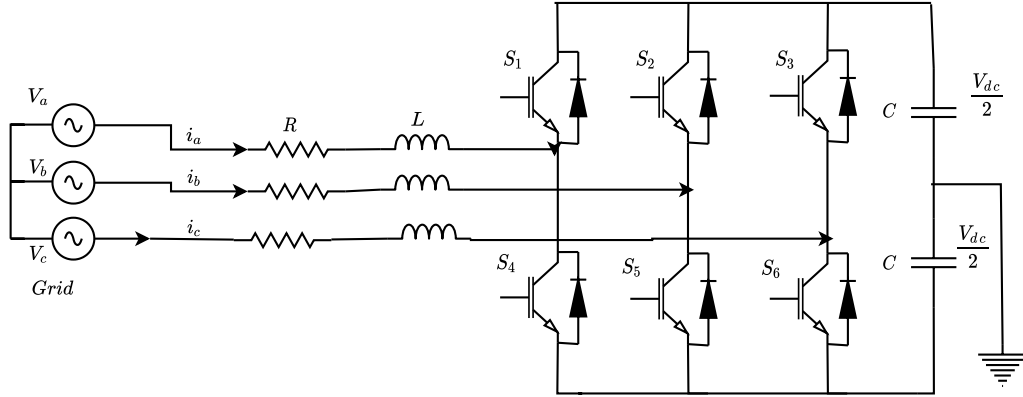


Figure 2-5: Three-phase rectifier showing switches, input reactor and DC-link capacitor

Similarly, for phases b and c, the equations can be obtained respectively as:

$$V_b = Ri_b + L \frac{di_b}{dt} + \frac{V_{dc}}{2} d_b, \quad (2-16)$$

$$V_c = Ri_c + L \frac{di_c}{dt} + \frac{V_{dc}}{2} d_c, \quad (2-17)$$

where d_a , d_b , and d_c denote the average value of the on state of the switches over one switching period. To investigate the dynamic response of the rectifier, (2-15) to (2-17) are rearranged to form differential equations

$$L \frac{di_a}{dt} = -Ri_a - \frac{V_{dc}}{2} d_a + V_a, \quad (2-18)$$

$$L \frac{di_b}{dt} = -Ri_b - \frac{V_{dc}}{2} d_b + V_b, \quad (2-19)$$

$$L \frac{di_c}{dt} = -Ri_c - \frac{V_{dc}}{2} d_c + V_c. \quad (2-20)$$

Meanwhile, no load is connected to the power converter. The instantaneous current flowing into the capacitor can be expressed as a function of the line currents and switching functions for each phase leg which is verified by

$$C \frac{dV_{dc}}{dt} = \frac{1}{2} (i_a d_a + i_b d_b + i_c d_c). \quad (2-21)$$

Assuming a balanced system, the sum of phase currents and duty ratios are given respectively by

$$i_a + i_b + i_c = 0, \quad (2-22)$$

$$d_a + d_b + d_c = 0. \quad (2-23)$$

By rewriting (2-22) and (2-23) to determine c-components in terms of a and b-components and substitute in (2-15) to (2-21) to get a simplified representation

$$\frac{d}{dt} \begin{bmatrix} i_a \\ i_b \\ V_{dc} \end{bmatrix} = \begin{bmatrix} -\frac{R}{L} & 0 & -\frac{d_a}{2L} \\ 0 & -\frac{R}{L} & -\frac{d_b}{2L} \\ \frac{d_a + d_b}{C} & \frac{d_b + d_a}{C} & 0 \end{bmatrix} \begin{bmatrix} i_a \\ i_b \\ V_{dc} \end{bmatrix} + \frac{1}{L} \begin{bmatrix} V_a \\ V_b \\ 0 \end{bmatrix} \quad (2-24)$$

that expresses a third order dynamic model of the three-phase rectifier.

In this thesis, a cascaded control structure involving a relatively slow outer voltage loop and a relatively fast inner current loop is adopted. To facilitate the analysis, it is necessary to break the model of the VSC into two parts that consists of one voltage dynamic equation and two current dynamic equations.

In addition, for the same reasons as synchronous generator, dynamic model of the rectifier is transformed from the stationary frame of reference to synchronously rotating frame of reference using Park's transformation. The assumption of a balanced system allows a simplification of the (2-6) to a two by two matrix expressed as [19]:

$$T_{dq/ab} = \sqrt{\frac{2}{3}} \begin{bmatrix} \cos \theta & -\sin \theta \\ \sin(\theta - \frac{\pi}{6}) & \cos(\theta - \frac{\pi}{6}) \end{bmatrix}. \quad (2-25)$$

Taking only current dynamic equations from (2-24) and applying (2-7) yields

$$L \frac{d}{dt} \begin{bmatrix} T_{dq/ab} \begin{bmatrix} i_d \\ i_q \end{bmatrix} \end{bmatrix} = -R \begin{bmatrix} 1 & 0 \\ 0 & 1 \end{bmatrix} T_{dq/ab} \begin{bmatrix} i_d \\ i_q \end{bmatrix} - \frac{V_{dc}}{2} T_{dq/ab} \begin{bmatrix} d_d \\ d_q \end{bmatrix} T_{dq/ab} \begin{bmatrix} V_d \\ V_q \end{bmatrix}. \quad (2-26)$$

With matrix differentiation property, applying (2-8) and after some simplification, the dynamic response of line current in synchronous rotating dq0 frame can be expressed as:

$$L \frac{d}{dt} \begin{bmatrix} i_d \\ i_q \end{bmatrix} = \begin{bmatrix} -R & \omega L \\ -\omega L & -R \end{bmatrix} \begin{bmatrix} i_d \\ i_q \end{bmatrix} - \frac{V_{dc}}{2} \begin{bmatrix} d_d \\ d_q \end{bmatrix} + \begin{bmatrix} V_d \\ V_q \end{bmatrix} \quad (2-27)$$

where ω represents the angular velocity of the rotating reference frame.

Similarly, following the same principle, the dynamic response of output DC voltage across the capacitor in synchronous rotating dq0 frame can be expressed as:

$$C \frac{dV_{dc}}{dt} = \frac{1}{2} \begin{bmatrix} d_d \\ d_q \end{bmatrix}^T \begin{bmatrix} i_d \\ i_q \end{bmatrix} \quad (2-28)$$

2-2-2 DC-DC Converter

The output DC voltage of the voltage source converter of Figure 2-5 is usually higher than the DC voltage needed by the electrolyzer. Therefore, a DC-DC converter known as a buck-converter is applied between them to step down the output of rectifier to operating voltage of the electrolyzer. In addition, the DC-DC converter is essential to meet requirements in terms of output current ripples and energy efficiency of the electrolyzer [23]. In this thesis, a buck converter with averaged current mode control is considered and operates in Continuous Conduction Mode (CCM), assuming the difference between input voltage and output voltage is not too high [24]. Otherwise, the inductor component of the converter must be oversized which leads to an increase in the inductor volume, price and a decrease in energy efficiency. The architecture of the buck converter, seen in Figure 2-6, is implemented to derive its dynamic model which consists of ideal components such as an input voltage V_{in} , a main switch S, a freewheeling diode D, an output inductance L , an output capacitor C and an electrolyzer as a load R_L . When the switch S is on during time T_{on} , the power flows from the voltage source to the load via the output inductor as indicated by a blue line in the circuit

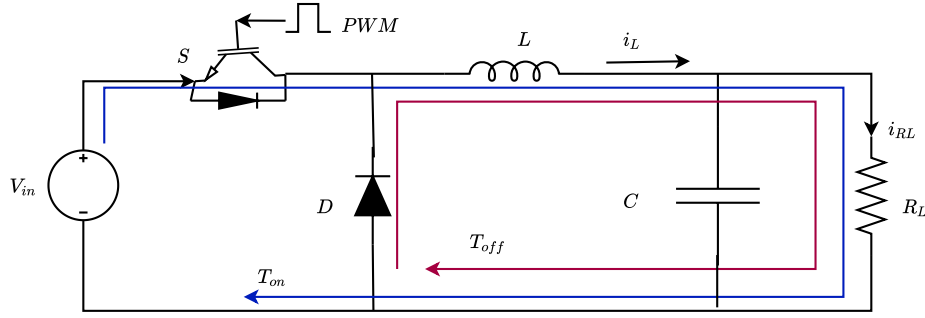


Figure 2-6: Classic buck converter

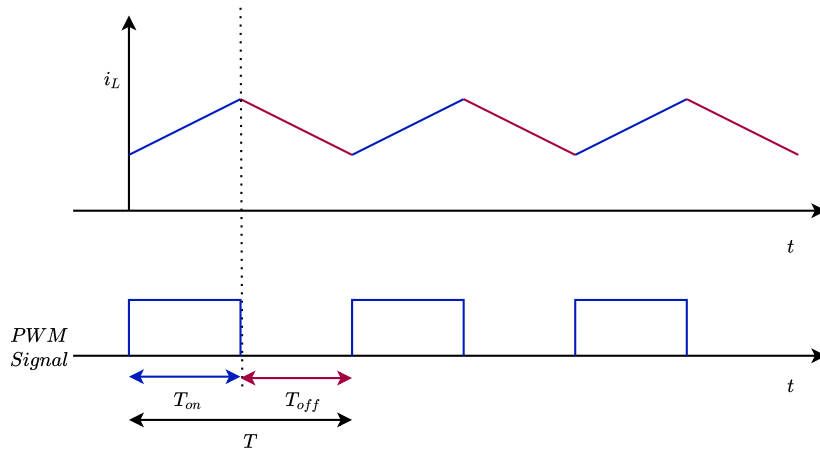


Figure 2-7: Inductor Current in the CCM

diagram. As a result, the inductor current i_L is increased. On the other hand, when the switch S is turned off during T_{off} , the load current, denoted by red line, flows through the diode D and the inductor current i_L is decreased. The waveform of inductor current i_L under CCM is provided in Figure 2-7.

Ignoring the inductor current ripple and capacitor voltage ripple, during on-state, the voltage on the inductor is given by

$$V_L = V_{in} - V_{RL}, \quad (2-29)$$

and then inductor current i_L at the end of the on-state can be determined by

$$\Delta i_{Lon} = \frac{1}{L} \int_0^{T_{on}} V_L dt = \frac{1}{L} \int_0^{T_{on}} (V_{in} - V_{RL}) dt = \frac{(V_{in} - V_{RL})T_{on}}{L}. \quad (2-30)$$

The ratio of the on-state time T_{on} to the period T of the switching signal is called duty ratio D . Therefore, (2-30) can be rewritten as.

$$\Delta i_{Lon} = \frac{(V_{in} - V_{RL})DT}{L}. \quad (2-31)$$

During off-state, inductor current flows through the load and diode where $V_L = -V_{RL}$, since $\frac{di}{dt} < 0$. Therefore, the current can be calculated as :

$$\Delta i_{Loff} = \frac{1}{L} \int_{DT}^T -V_{RL} dt = -\frac{V_{RL}(1-D)T}{L}. \quad (2-32)$$

It can be observed from Figure 2-7 that the current i_L at the end of the off-state is the same as the value of it at the beginning of the on-state. Thus,

$$\Delta i_{Lon} + \Delta i_{Loff} = 0. \quad (2-33)$$

Substituting the variables Δi_{Lon} and Δi_{Loff} by their corresponding formulas from (2-30) and (2-32), (2-33) is modified to give

$$V_{RL} = DV_{in}. \quad (2-34)$$

It is proved by (2-34) that the output voltage of the buck converter is always less than the input voltage. In DC-DC converter with current mode control, its dynamic response is determined by the inductor current. The filter inductance is usually large in its work, which can be considered as a current source [24]. As no current is flowing through the output capacitor at steady state condition, the inductor current i_L can be determined by

$$i_L = \frac{DV_{in}}{R_L}, \quad (2-35)$$

which shows that the inductor current has linear relationship with the duty ratio D and load R_L .

Whereas at transient state, the current via the inductor is the sum of the current through the capacitor C and electrolyzer load R_L which can be expressed as:

$$i_L = i_{RL} + C \frac{dV_{RL}}{dt} = i_{RL} + CR_L \frac{di_{RL}}{dt}. \quad (2-36)$$

Applying Laplace transform on (2-36) yields the open loop transfer function of the converter that is calculated as :

$$G_{iL}(s) = \frac{i_{RL}}{i_L} = \frac{\frac{1}{CR_L}}{s + \frac{1}{CR_L}}. \quad (2-37)$$

The values of the output filter inductance and capacitance of the buck converter can be estimated, if the PWM period T , the converter supply voltage V_{in} and the converter minimum current i_{min} as well as cutoff frequency f_{cmin} are known [25]. Having these values, the minimum inductance and maximum capacitance value of the converter are respectively obtained by

$$L > \frac{TV_{in}}{8i_{min}}, \quad (2-38)$$

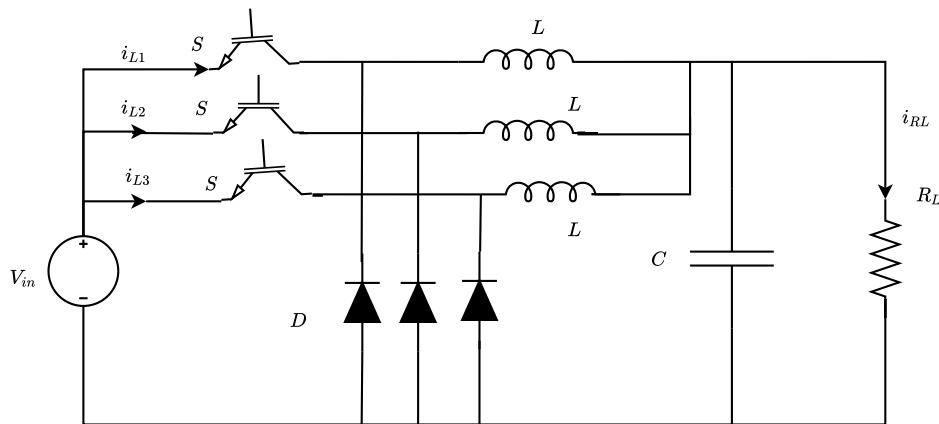
$$C \leq \left(\frac{1}{2\pi f_{cmin} \sqrt{L}} \right). \quad (2-39)$$

Different DC/DC converter configurations can be used depending on the feature of the electrolyzer and electrical grid. The different DC/DC converter topologies are compared in [26] in

Table 2-1: Comparison of DC-DC Converter

Converters	Ripple	Efficiency	Cost	Reliability	Volt-ratio
Classical	unacceptable	medium	acceptable	unacceptable	Medium
Double quadratic	acceptable	acceptable	medium	acceptable	medium
Interleaved	acceptable	acceptable	unacceptable	acceptable	acceptable
Half-bridge	acceptable	acceptable	medium	unacceptable	acceptable
Full-bridge	medium	acceptable	unacceptable	acceptable	medium

terms of their output current ripple reduction, conversion ratio, energy efficiency, and power switch fault-tolerance. From the comparison of some types of buck converters shown in Table 2-1, interleaved DC/DC converter seems to be the most attractive topology for electrolyzer applications. It is developed from classic buck converter to increase power level by sharing the current between different legs [27]. This topology consists of several buck Converters sharing a common DC bus. The N number of PWM gate control signals are shifted from each other by $360^\circ/N$ in order to minimize the output current ripple and the passive component volume. For optimization reasons in terms of magnetic components volume, output current ripple reduction and energy efficiency optimization, the 3-leg interleaved buck converter shown in Figure 2-8 tends to be the best candidate. It can also be observed that such converter could be available in case of a power switch failure.

**Figure 2-8:** 3-leg interleaved buck converter

2-3 Electrochemical Model of PEM Electrolyzer

Hydrogen is the simplest and lightest chemical element of the periodic table. Even though hydrogen is the most abundant element in the universe, it cannot be found in its pure state in the nature. Therefore, it must be produced from other chemicals by means of energy input. There are several resources available for hydrogen production such as fossil fuels (e.g. natural gas and coal) and RES (e.g. biomass and water). Although the flexibility, high energy

density and high storage capacity potential of hydrogen is superior to other energy carriers and storage technologies, the International Renewable Energy Agency (IRENA) recently reported that globally only about 4% of hydrogen production is through water electrolysis [28]. The remainder of the hydrogen is produced through processes like steam-methane reforming, oil gasification and coal gasification from fossil fuel. The main reasons for the low amount of hydrogen produced through water electrolysis include the high capital expenditure (CAPEX) and operating expense (OPEX) of these systems [29].

From an environmental point of view, the hydrogen production from fossil fuels contributes considerably to the release of greenhouse gases and other pollutants into the atmosphere, even though it does save money [27]. A high-quality hydrogen (almost 100% hydrogen) can be produced by an electrochemical conversion of water to hydrogen and oxygen through a process known as water electrolysis [30]. Thus, this thesis focuses mainly on the production of green hydrogen from renewable energy sources by means of electrolysis due to its environmental friendly process.

2-3-1 Water Electrolysis Technologies

Water electrolysis technologies can be classified according to the applied electrolyte, which separates the two half reactions at the anode (oxidation reaction) and cathode (reduction reaction) of the electrolyzer [31]. The four main types of water electrolyzers exist at the moment are Anion Exchange Membrane (AEM) electrolyzer, Solid Oxide Electrolyzer (SOE), alkaline electrolyzer and Proton Exchange Membrane (PEM) electrolyzer.

AEM electrolyzer: is the newest electrolyzer technology where the two electrodes of the electrolyzer are separated by the AEM made up of non-fluorinated hydrocarbon based membrane [32]. The electrolysis system generally consists of an alkaline and non-noble metal electrocatalysts for both the anode and the cathode. According to [33], AEM electrolyzer has thin membrane that offer includes reduced mass transport resistance and ohmic resistance.

SOE electrolyzer: is a pilot project that has attracted a great deal of interest, because it can convert electrical energy into chemical energy, producing hydrogen with a high efficiency. According to [31], SOE is also interesting due to high temperature of operation which results improved kinetics, thermodynamics favoring internal heat utilization and the conversion of steam. The SOE technology has a huge potential for the future mass production of hydrogen, if the issues related to the durability of the ceramic materials at high temperature and long-term operation are solved.

Alkaline electrolyzer: is a well matured technology for hydrogen production up to the megawatt range and constitutes the most extended electrolytic technology at a commercial level worldwide [34]. It is characterized by having two electrodes immersed in a liquid alkaline electrolyte consisting of a caustic potash solution of potassium hydroxide (KOH). The two electrodes are separated by a diaphragm which has the function of keeping the product gases apart from one another for the sake of efficiency and safety.

PEM electrolyzer: is referred to as proton exchange membrane or polymer electrolyte membrane (both with the acronym PEM) water electrolysis and less frequently as solid polymer electrolyte (SPE) water electrolysis. The polymer electrolyte membrane (Nafion, fumapem) is responsible for providing high proton conductivity, low gas crossover, compact system design and high pressure operation [30]. The low membrane thickness is in part the reason for many of the advantages of the solid polymer electrolyte.

From Table 2-2 of comparison of the water electrolysis technologies, it can be observed that PEM is favored due to its higher power density, compact system design, improved hydrogen purity and sufficient partial load range compared to alkaline electrolyzer [31]. In addition, it has faster dynamic performance and flexibility to provide primary and secondary power reserves compared to the AEM and SOE pilot electrolyzers. Therefore, the electrochemical characteristics of the PEM electrolyzer is studied in this thesis for the grid-support analysis.

Table 2-2: Water Electrolysis Technologies Comparison

Parameters	Alkaline	PEM	SOE	AEM
Electrolyte	KOH	Nafion	Ceramic	Polysulfone
Plant η (%)	60-70	70-80	>95	80-90
Maturity	Well matured	Commercial	Lab. stage	Pilot project
Gas-purity	Low degree of purity	high gas purity	unknown	unknown
Cost	Low cost	High cost	No cost info.	Low
Partial-load	Low range	Good range	unknown	unknown
Stack power level	MW range	below MW	kW range	unknown
Pressure	Low	Medium	High	unknown
System response	Low	rapid	unknown	rapid
Current density	Low	High	unknown	Medium
Catalyst	Non noble	Noble	non noble	non noble

2-3-2 V-I characteristics of PEM Electrolyzer

The basic internal structure of a PEM device consists of porous electrodes separated by a solid electrolyte membrane, usually Nafion. A catalyst layer is situated between the electrolyte and the electrodes made of platinum(Pt) for the cathode and iridium(Ir) for the anode. In addition, an external electrical circuit is connected across the electrodes. The electrolyte layer allows the transfer of only hydrogen ions (protons), while the electrons flow through the external circuit. This structure is shown in Figure 2-9. The solid polymer electrolyte membrane guarantees a low gas crossover, allowing the PEM electrolyzer to work under a lower partial load range (0–10%), and it can have a compact design. This allows the obtaining of high enough operating pressures (30–40 bar), as an effect of the electrochemical compression in PEM technology, to directly fill the pressure hydrogen storage tanks [5].

The water electrolysis operation is an electrolytic process which decomposes water H_2O molecule via a reduction oxidation (redox) reaction into oxygen O_2 and hydrogen H_2 gases with the help of an electric current. The reaction including the thermodynamic energy values

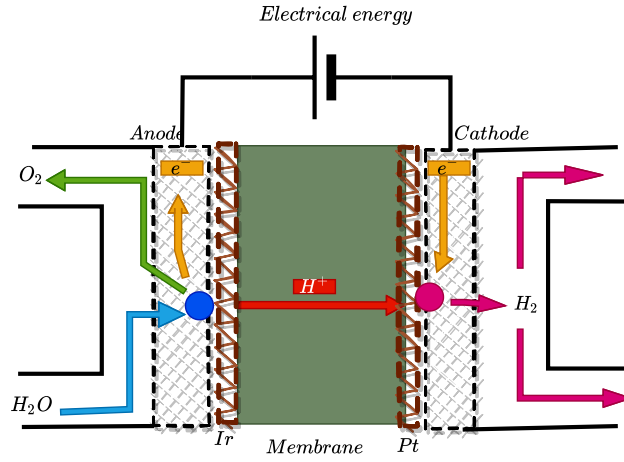
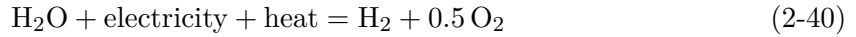


Figure 2-9: Schematics of PEM electrolyzer device

is described as:



An oxidation describes donation of electrons by molecules, atoms or ions. Such reaction occurs at the anode that can be expressed by a chemical formula as :



where water is decomposed to produce oxygen molecules, electrons and hydrogen ions. As it can be seen in Figure 2-9, after the oxidation reaction, the electrons flow to the cathode side through the outer loop of the electrode, whereas the hydrogen ions move to the cathode side via the polymer electrolyte membrane. Reduction deals about the opposite reaction of oxidation where electrons are uptaken by atoms, molecules or ions. In water electrolysis, the transferred electrons and hydrogen ions react to form hydrogen molecule in the cathode side and can be written by a chemical formula as:



For splitting the water molecule, the electric energy is consumed by the redox chemical reaction. The energy to initiate the electrolysis at a constant temperature and pressure is determined by the enthalpy change ΔH of the process. Part of this energy is electrical and equal to Gibbs energy ΔG ; the rest is thermal energy Q and equals to the product of the process temperature T and the entropy change ΔS [35]. Assuming that the temperature of the PEM electrolyzer cell is given in Kelvin [k], the change in enthalpy for the water splitting can be given according to the following equation:

$$\Delta H = \Delta G + T\Delta S. \quad (2-43)$$

Using the energy change equation (2-43) and an electrochemical process aspect, the electrolyzer model could be divided into an electrical model and a thermal model. The electrical model is based on the energy exchange in link with the Gibbs energy and the electric source,

whereas the thermal model is composed by the energy generated by entropy and the energy lost (or gained) by the external temperature and chemical components' movement [36]. This thesis covers only the electrical model that is deduced from an algebraic relation between the cell current I and the cell voltage V . I–V curve is highly dependent on the electrolysis process temperature, but slightly dependent on process pressure [31]. For a given temperature T and pressure P , the current density versus cell voltage relationship can be demonstrated using a polarization curve (PC) or an electrochemical impedance spectroscopy (EIS). The PC is a plot of the cell voltage as a function of the current density at constant operating conditions (temperature and pressure). The PC was obtained by operating the cell over a range of current densities and measuring the cell voltage at each current density. The EIS, on the other hand, is an analytical technique used to characterize an electrochemical cell by obtaining the impedance of the cell as a function of frequency [37]. In this case, the PC is used to benchmark an electrolyzer and indicate the different loss regions within the electrolyzer as shown in Figure 2-10.

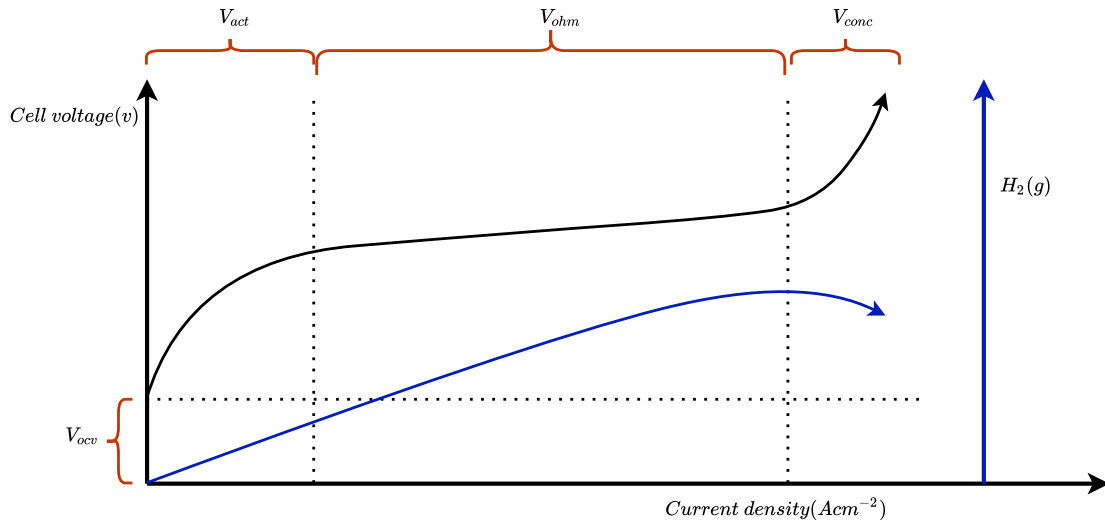


Figure 2-10: Polarization curve of PEM electrolyzer

When an input voltage is applied to a PEM cell, several voltage drops appear described as operating cell voltage V which is determined by the sum of an open-circuit voltage V_{ocv} , an activation overpotential V_{act} , an ohmic overpotential V_{ohm} and a concentration overpotential V_{conc} . The level of the effect of each overpotential on I–V characteristics of the PEM electrolyzer is indicated in Figure 2-10.

$$V = V_{ocv} + V_{act} + V_{ohm} + V_{conc} \quad (2-44)$$

Open Circuit Voltage (OCV): is caused by the chemical redox reaction at the first stage of the process that represents the cell potential when the current is nil [36]. It can be defined

by the Nernst equation as:

$$V_{ocv} = V_0(T) + \frac{RT}{zF} \ln \frac{P_{H_2} P_{O_2}^{0.5}}{P_{H_2O}}, \quad (2-45)$$

where R is universal gas constant, F denotes Faraday constant, z indicates number of valency electrons, T represents temperature, P_{H_2O} , P_{H_2} and P_{O_2} in atm are respectively the universal gas constant, the Faraday's constant, electron moles, stack temperature, the partial pressures of water, hydrogen and oxygen. The stack must operate at a hydrogen pressure of at least a 0.068 bar above the water pressure. This is to ensure that hydrogen can be detected in the water/oxygen outlet in the event a membrane is breached (membrane failure) [5]. In this case, a pressure difference of 1 bar is implemented between the cathode (35 bar) and anode (34 bar).

The minimum voltage required to initiate the electrolysis is represented by V_0 which can be defined using the change in the molar Gibbs free energy of water reaction formation. By rearranging (2-43), the reversible voltage is a function of temperature expressed as:

$$V_0(T) = \frac{\Delta G}{zF} = \frac{\Delta H - T\Delta S}{zF}. \quad (2-46)$$

According to [38], if the thermal energy $T\Delta S$ is supplied by electricity, as it is the case in most commercial electrolyzers, the minimum voltage to start the electrolysis is referred to as the thermoneutral voltage V_t is given by

$$V_t = \frac{\Delta H}{zF}. \quad (2-47)$$

At standard temperature and pressure conditions (298.15 K and 1 atm), $\Delta G^0 = 237.21$ kJ mol⁻¹ and $\Delta H^0 = 285.84$ kJ mol⁻¹ [38]. Substituting these terms in (2-46) and (2-47) the reversible and thermoneutral voltages at standard conditions are obtained as: $V_{std} = 1.229$ V and $V_{tn} = 1.481$ V respectively. According to [30], to adjust the OCV from standard temperature, the reversible voltage $V_0(T)$ can be calculated using an empirical relation

$$V_0(T) = V_{std} + 0.9 * 10^{-3}(T - 298.15). \quad (2-48)$$

Activation overpotential: is caused by activation phenomena related to the electrochemical kinetics of the anode and cathode simultaneous half-reactions [36]. The electric charge transferred between the chemical species and the electrodes requires energy. The energy step that the charge must overcome to go from the reactants to the electrodes and vice versa is referred to as activation energy and highly depends on the electro-catalytic properties of the electrode materials [38]. However, the interface electrode-electrolyte, where the electrical transfer takes places, behaves as a dielectric during the redox half-reactions speed changes. As a consequence, an overcharge appears on the electrode surface that is compensated by the accumulation of ions of opposite polarity in the electrolyte. These two layers of opposite charge are referred to as the double-layer effect and are the main cause of the dynamic electrical behavior of an electrolyzer.

Modeling this phenomenon accurately can be challenging as material processing, temperature, active catalyst areas, utilization, distribution, age, pressure, morphology, and many other parameters are very difficult to quantify, as all play a role [30]. The electrochemical model

used throughout both the fuel cell and electrolyzer communities to describe the activation overpotential is referred to as the Butler-Volmer equation [39]

$$V_{act} = V_{act,a} + V_{act,c} \quad (2-49)$$

$$V_{act} = \frac{RT}{2F} \left(\frac{1}{\alpha_a} \operatorname{arcsinh} \left(\frac{i}{2i_{0,a}} \right) + \frac{1}{\alpha_c} \operatorname{arcsinh} \left(\frac{i}{2i_{0,c}} \right) \right), \quad (2-50)$$

where $\alpha_{a,c}$ stands for charge transfer coefficient, $i_{0,a,c}$ denotes exchange current density and i represents instant current density. The magnitude of the cathode activation overpotential is much smaller than the anode activation overpotential, because kinetics of the hydrogen evolution reaction at cathode are faster than kinetics of the oxygen evolution reaction at anode [39]. Therefore, (2-50) is deduced to determine only anode activation overvoltage, neglecting the cathode side.

Ohmic overpotential: corresponds to the product of the ohmic losses and the circulating current i_{ely} within the cell. It is mainly the consequence of the resistance R_{elec} to the electron flux due to the electrodes, the bipolar plates, the current collectors and their interconnections, as well as the resistance R_{mem} that the electrolyte and the diaphragm oppose to the ion flux [38]. Mathematically, it can be expressed applying Ohm's law as:

$$V_{ohm} = (R_{elec} + R_{mem})i_{ely}. \quad (2-51)$$

Components of the cell that cause electronic resistance are too complicate to model as well as they have negligible contribution (ten times lower) compared to protonic resistance [39]. Thus, this study is considering only the ionic resistance that is determined by the ratio of membrane thickness δ_{mem} to the membrane protonic conductivity σ_{mem} . Many approaches exist to modeling proton conductivity through the membrane, most of which have been developed for the modeling of fuel cells. According to [30], a very commonly used empirical relation σ_{mem} for the membrane conductivity is using an Arrhenius expression

$$\sigma_{mem} = \sigma_{mem,std} \cdot \exp \left(\frac{-E_{pro}}{R} \left(\frac{1}{T} - \frac{1}{T_{std}} \right) \right), \quad (2-52)$$

where E_{pro} is the activation energy required for the proton transport in membrane and $\sigma_{mem,std}$ is the membrane conductivity at the standard temperature and pressure condition.

Concentration overpotential: predicts the voltage loss due to a surplus of reaction products at the catalyst sites blocking the reactants in electrodes. At very high current densities, bubbles of gases are not removed from electrodes as fast as they are produced, which involves various negative impacts, such as variations of partial pressures and chemical reaction velocity, that decrease the electrolyzer efficiency [36]. Thus, most electrolyzer manufacturers nominate certain range of operating current density depending on the materials used and operating conditions. In this case, a maximal operating point of current density of 1.43 A/cm^2 is applied based on [39] which is controlled by the power converters associated to the electrolyzer, so that the concentration overvoltage would not affect the electrolysis process.

Most of the PEM electrolyzers operate at a stack level that is formed from a series connection of number of cells. The above-mentioned derivation and simplification of cell level open circuit voltage and overpotentials are also applicable for the PEM stack except being multiplied by

number of cells N_c . Therefore, the stack voltage V_{ely} is developed by Substituting (2-45)-(2-52) in the over all cell voltage expression Eq. (2-44) to give

$$V_{ely} = N_c (V_{ocv} + V_{act} + V_{ohm}),$$

$$V_{ely} = N_c \left(V_0(T) + \frac{RT}{zF} \ln \frac{P_{H_2} P_{O_2}^{0.5}}{P_{H_2O}} + \frac{RT}{2F} \left(\frac{1}{\alpha_a} \operatorname{arcsinh} \left(\frac{i}{2i_{0,a}} \right) \right) + \frac{\delta_{mem} \cdot i_{ely}}{\sigma_{mem,std} \cdot \exp \left(\frac{-E_{pro}}{R} \left(\frac{1}{T} - \frac{1}{T_{std}} \right) \right)} \right), \quad (2-53)$$

where the values of the parameters α_a , $i_{0,a}$, δ_{mem} , $\sigma_{mem,std}$ and E_{pro} , listed in Table 1, are taken from [39] which are determined by non-linear fitting of the electrolyzer's polarization curves using the Particle Swarm Optimization algorithm.

The electrical circuit representation of the PEM electrolyzer shown in Figure 2-11 is derived from the aforementioned open circuit voltage and overpotentials explanations. The open circuit voltage is denoted by a constant voltage V_{ocv} , the ohmic overpotential is due to the membrane resistor R_{mem} circuit and the parallel connection of the variable charge transfer resistance R_{act} and double layer capacitance C_{DL} denote the cause of the activation overpotential which is a nonlinear current dependent. The simplified electrochemical of electrolyzer is connected to the grid via a power electronics interface as seen in Figure 2-11.

The nonlinearity of the PEM electrolyzer is due to the RC element of the equivalent electric circuit at which the first order differential equation describing the activation overpotential V_{act} on the anode-electrode is derived from transient current flowing via the capacitor expressed as:

$$\frac{dV_{act}}{dt} = \frac{1}{C_{DL}} \left(i_{ely} - \frac{1}{R_{act}} V_{act} \right). \quad (2-54)$$

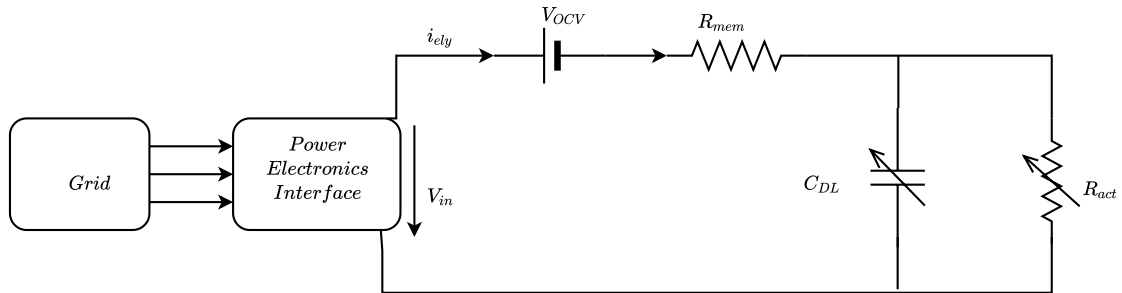


Figure 2-11: Proposed electrolyzer stack model and grid interface

2-4 Balance of Plant of PEM Electrolyzer

The BoP represents all supporting components and auxiliary systems assembled for the proper operation of PEM electrolyzer and capable the stack to run at its best performance. Its structure and size depends on the level of the electrolyzer. For optimal design of the BoP, it's categorized into subsystems as shown in Figure 2-12 with different colors that includes the

power supply subsystem, water management subsystem, hydrogen production subsystem, cooling subsystem and control subsystem [40].

The stack power supply subsystem marked with green color is responsible for providing the necessary direct current for the electrolysis process to produce hydrogen. This subsystem is explained and modeled in the aforementioned subsections as well as in the preceding chapters of the thesis.

The water management subsystem colored with blue guarantees the proper water supply to the electrolyzer. It is comprised with several components such as, deionized water tank which is convenient to have low conductivity and ensures longer stack lifespan, injection pump to ensure an adequate input flow, an oxygen separator tank that acts as a sink for wastewater and separator for oxygen from water, recirculation phase regulates the water flow to fulfill all the critical water parameters before being injected into the PEM electrolyzer.

The hydrogen production subsystem indicated with red color is carefully designed to guarantee all the safety parameters, the correct hydrogen drying, eliminating the humidity that it may contain and sending the extracted water to the oxygen separator tank. The hydrogen produced on the cathode side of PEM electrolyzer is transported to the High Pressure Separator (HPS) tank of this subsystem to be separated into wet hydrogen(dirty H₂) and dry hydrogen(clean H₂) and transferred to Low Pressure Separator (LPS) tank and Pressure Swing Adsorption (PSA) respectively. The LPS tank is used to release dirty H₂ to air and send wastewater to oxygen separator tank. On the other hand, the PSA Further dries the clean hydrogen before filled to storage tank. Nitrogen gas(N₂) is injected to the pipelines of this subsystem before the start and after the end of hydrogen production to remove or inertize any residual gas in the pipelines.

The cooling subsystem with orange regulates the operational temperature of the electrolysis process at certain range by controlling the electro-valves of the injected water and the produced hydrogen into and out of the membrane electrode assembly respectively. The water for the heat exchangers is cooled by an external air cooler which has its own pump to guarantee water flow and pressure in the cooling line.

The gray colored control subsystem processes all the information received from sensors, and based on the user-defined parameters and the control logic defined, it automatically acts over actuators to put the system working at the proper operating state. All the above subsystems are controlled and communicated with the front end controller of power converters of PEM electrolyzer through this subsystem.

In order to capture the full electrical response of PEM electrolyzer, it is important to model these components of BoP. The previous explanations of the subsystems show that the electrical response could be due to electronic loads and circulation pumps. The electronic loads represent control systems of BoP and have fixed power consumption, whereas the circulation pumps require an electrical power for a proper operation that can be determined by

$$P_{pump} = \frac{Q\Delta P}{36\eta} \quad (2-55)$$

where P_{pump} is the electrical power input to the motor in W, Q is the pump capacity in m³/h, ΔP denotes the pressure differential in bar and η is the combined efficiency of the motor, transmission and pump [41]. If the circulation pumps are assumed to have fixed efficiencies and fixed pressure difference, then their power consumption is constant.

According to [42], there are two ways of load modeling: dynamic and static. Dynamic load modeling expresses the active and reactive powers of a load as a function of voltage and time

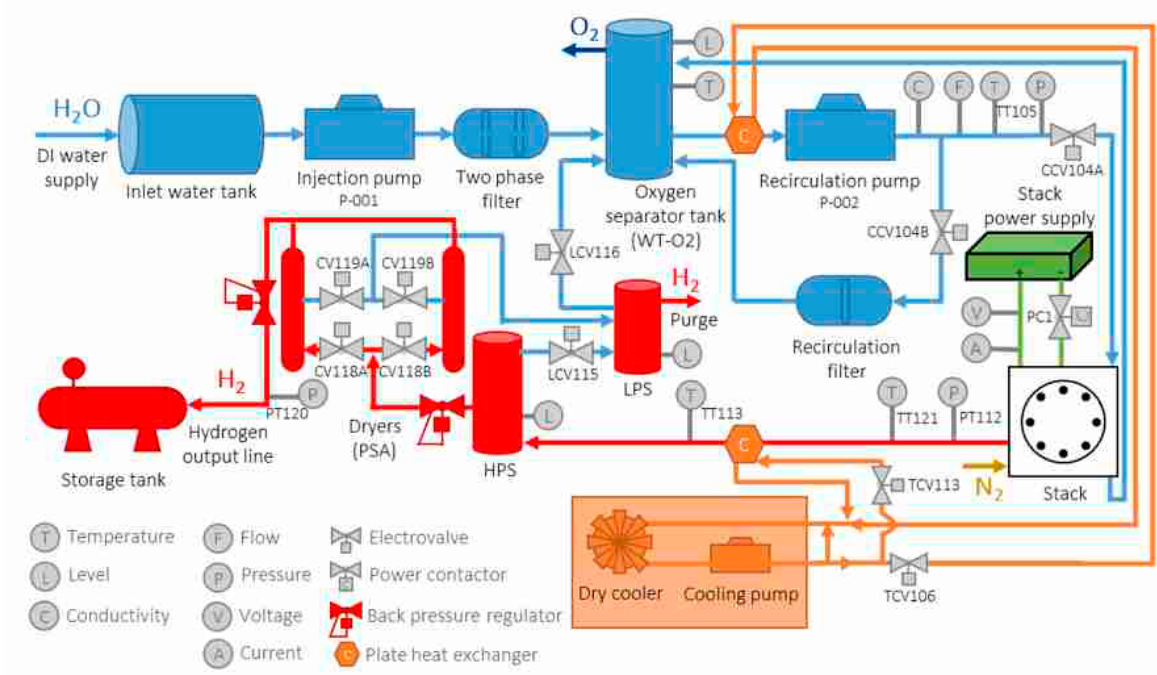


Figure 2-12: BoP of a PEM electrolyzer: blue-water management subsystem, red-hydrogen production subsystem, yellow-cooling subsystem. Extracted from [5]

(e.g., induction motor). On the other hand, static load modeling expresses the active and reactive power of a load at any instant of time as functions of bus voltage magnitude and frequency. Thus, the BoP of PEM electrolyzer is represented by a static model as they are assumed to have a constant power consumption.

The voltage dependency of load characteristics of BoP can be represented by an exponential model as:

$$P_{BoP} = P_{BoP0} \left(\frac{V}{V_0} \right)^a, \quad (2-56)$$

$$Q_{BoP} = Q_{BoP0} \left(\frac{V}{V_0} \right)^b, \quad (2-57)$$

where P_{BoP} and Q_{BoP} are respectively the active and reactive components of the load power consumption when the bus voltage is V . The subscript 0 identifies the value of the respective variables at the initial condition. In addition, the exponent a and b represent the voltage dependent parameter of the active and the reactive power respectively.

The frequency dependency of load characteristics of BoP is usually represented by multiplying the exponential model by a factor as follows,

$$P_{BoP} = P_{BoP0} \left(\frac{V}{V_0} \right)^a (1 + K_{pf} \Delta f), \quad (2-58)$$

$$Q_{BoP} = Q_{BoP0} \left(\frac{V}{V_0} \right)^b (1 + K_{qf} \Delta f), \quad (2-59)$$

where Δf is the frequency deviation, whereas K_{pf} and K_{qf} are the frequency sensitivity coefficients for active and uncompensated reactive power load respectively.

The overall efficiency of the whole system for the hydrogen production is the ratio of the power generated in the form of hydrogen P_{H_2} to the sum of electrical power P_{elec} input to the stack and power consumed by BoP P_{BoP} and is expressed as:

$$\eta_{sys} = \frac{P_{H_2}}{P_{elec} + P_{BoP}}. \quad (2-60)$$

Where P_{H_2} and P_{elec} are obtained using (3-39)-(3-43), whereas the power consumption of BoP is estimated as 10% of the total load for an electrolyzer in the range from 1 to 2 MW. Finally, the system efficiency is lower than the stack efficiency which reaches up to 61%. By contrast, BoP components are fed from a separate AC supply as shown in Figure 2-13 and operate at steady state and are therefore not impacted by the demand set point changes sent to the electrolyser for grid stability.

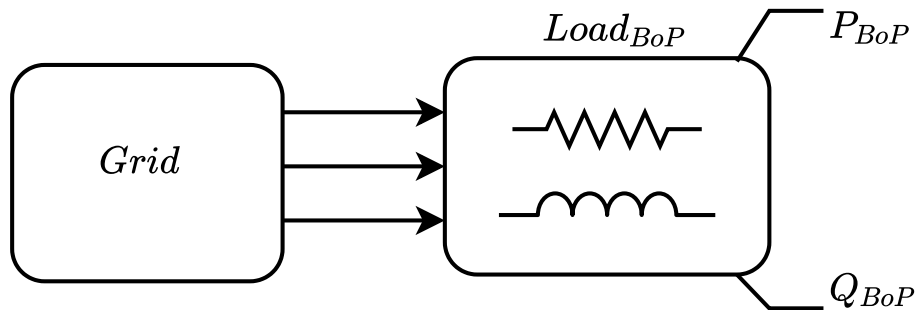


Figure 2-13: Balance of plant load model

Control Methodology

In general, the main objective of a control scheme in power system is to generate and deliver power in an interconnected system as economically and reliably as possible, while maintaining the voltage and frequency within permissible limits [14]. In this case, the feasibility of grid-support with electrolyzer depends on the control scheme put in place. This chapter describes the hierarchical control design which translates external signals into low level reference signals for converters in the power conversion system. The discussion starts with a simplified control design of a synchronous generator for a proper representation of a grid, and proceeds with a hierarchical control scheme of power converters as well as the power-to-gas conversion system.

3-1 Control of the Synchronous Generator

The frequency of a power generation is mainly affected by an active power difference between a generator and a load demand, but less sensitive to reactive power changes. On the other hand, the voltage magnitude of the synchronous generator is particularly affected by a reactive power deviation rather than the active power variation in a grid [3]. Thus, the cross-coupling between the frequency control loop and voltage regulator is negligible. Hence, frequency control and voltage control can be analyzed independently. Figure 2-4 shows an illustration of the interplay between a Synchronous Machine (SM) model, a frequency control system and a voltage regulator [4].

3-1-1 Frequency Control

The model being considered in this thesis consists of a frequency loop that captures the rotor dynamics. The frequency dynamics include those of the governor and turbine which dictate the evolution of the generator rotor angle [43]. As shown in Figure 2-4, they are respectively modeled by proportional speed droop control and first order turbine dynamics as follows:

$$p_g = p^* + \frac{1}{R_g}(\omega_0 - \omega), \quad (3-1)$$

$$\tau_g \dot{p}_g = p_g - p_m, \quad (3-2)$$

where p^* denotes the power set-point, p_g is the governor output power, R_g denotes the governor speed droop gain, and ω_0 as well as ω indicate the nominal and measured frequency respectively. Furthermore, τ_g denotes the turbine time constant and p_m represents the turbine output which is applied on generator to give the desired electrical output.

In this thesis the turbine is represented by Linear Time-invariant System (LTI) block that takes the output of the governor as its input and gives mechanical power to be delivered to the generator. Simulink's implementation of the whole load frequency control diagram interconnected with SM model is shown in Figure 3-1.

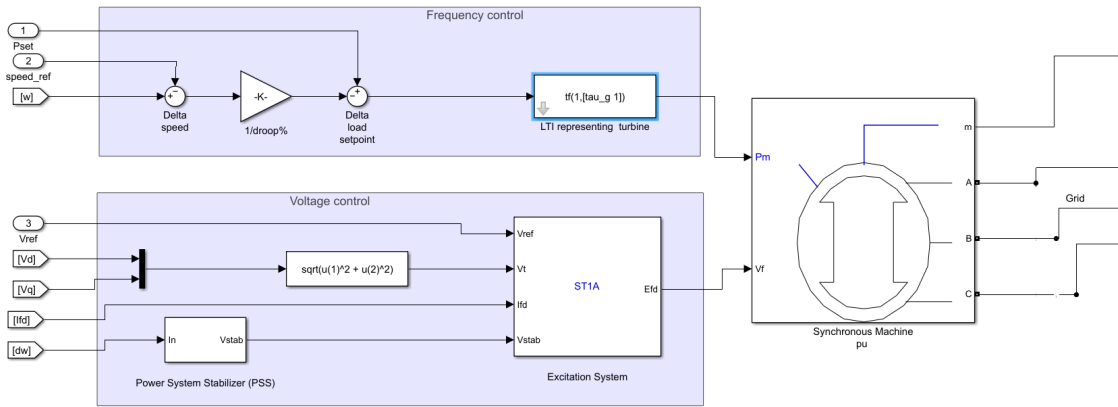


Figure 3-1: Simulink Blocks of a synchronous generator equipped with a prime mover, governor and voltage excitation system representation

3-1-2 Voltage Amplitude Control

The voltage and reactive power of a generator is defined by its excitation system. This means that the generator excitation regulation is actually the regulation of generator output energy and also impacts the stability of the entire electric power system.

An excitation current is provided by the excitation system, which, according to [44], usually consists of Automatic Voltage Regulator (AVR), exciter, measuring elements, Power System Stabilizer (PSS), limitation as well as protection unit as shown in Figure 2-4.

The exciter is the source of an electrical power for the field winding of generator and is controlled by the AVR, which is very effective during a steady-state operation. According to [45], in case of sudden disturbances however it may have negative influence on the damping of power swings, because it then forces field current changes in the generator. This may be eliminated by introducing a supplementary control loop PSS, which produces an additional signal into control loop to compensate voltage oscillations. PSS input quantities may be speed deviation, generator active power, frequency deviation, transient electromotive force and generator current.

Limitation and protection unit contains larger number of circuits which ensure that certain physical values (e.g. generator armature voltage, excitation current, etc.) are limited [46].

In this thesis, the system is augmented with a ST1A type of excitation dynamics with built-in AVR as demonstrated in Figure 3-1. To counteract the well-known destabilizing effect of the

AVR on the synchronizing torque, the system is equipped with a simplified PSS comprised of a two-stage lead-lag compensator [16].

3-2 Control of Power Converters

This section describes the hierarchical control scheme of converters in the power conversion system. The main objectives of the control scheme are to maximize hydrogen production and enable ancillary service capabilities in a stable manner. The proposed scheme in this thesis retains a simple structure which allows manipulation of the target system variables to achieve the above stated objectives. The scheme, which enables controlled exchange of active and reactive power between the electrolyzer and the power system has two levels: the lower level (rectifier and buck converter) controls which are covered in this section and the upper level (grid-support) control that will be described in Chapter 4.

3-2-1 Internal Model Control

Internal Model Control (IMC) is a method for control design, for which the resulting controller becomes directly parameterized in terms of plant model parameters and the desired closed loop bandwidth [47]. The controller structure for power converters in this thesis is based on this control approach. Figure 3-2 represents a general schematic diagram of IMC, in which $G(s)$ is the process to be controlled, $\hat{G}(s)$ is a model of the process (either exact or approximate), $d(s)$ is the disturbance and $r(s)$ is the reference signal. This philosophy is described in detail in [48]. Applying this principle yields the controller transfer function in the form:

$$F(s) = \frac{\alpha^n}{(s + \alpha) - \alpha^n} \hat{G}^{-1}(s), \quad (3-3)$$

where $F(s)$ stands for transfer function of the controller, α denotes bandwidth of the controller and n denotes order of $\hat{G}(s)$. According to [49], this approach can result in poor load disturbance rejection and instability, for plants with zeros in the right half plane. The approach also assumes the plant is accurately modelled, which is not always the case in reality.

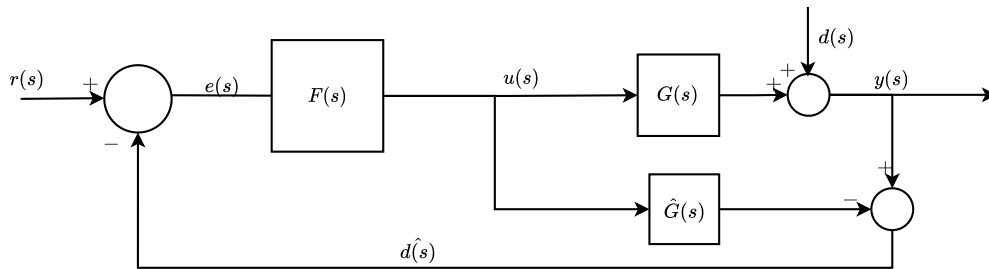


Figure 3-2: General schematic diagram of IMC

3-2-2 Control of Rectifier

As stated in subsection 2-2-1, in order to control the three-phase rectifier, a cascaded control structure involving relatively a decade slower outer voltage loop than inner current loop is adopted in this thesis. Thus, control functions are realized with a nested loop architecture comprising an inner loop which enables stable and fast control of grid current, and an outer loop which sets the references for the inner loops such that performance objectives are realized [49].

Phase-Locked Loop (PLL): is used to synchronize the active rectifier with the corresponding AC grid, which provides an estimation of the phase angle of the voltage V_{pcc} at the Point of Common Coupling (PCC) [50]. As illustrated in [51], the dq frame of the AC grid voltage can be expressed as :

$$V_d = \hat{V} \cos(\omega_0 t + \theta_0 - \theta), \quad (3-4)$$

$$V_q = \hat{V} \sin(\omega_0 t + \theta_0 - \theta), \quad (3-5)$$

where \hat{V} is the AC voltage magnitude, ω_0 is the AC system frequency, θ_0 is the source initial phase angle and θ is the arbitrary phase angle of Voltage Source Converter (VSC). The main function of PLL is to fulfill $\theta = \omega_0 t + \theta_0$, so that the V_q in (3-5) becomes zero. This can be achieved by applying a classical feedback control loop, in which $\omega_0 t + \theta_0$ is the reference input, θ is the output, and $H(s)$ is the transfer function of the effective compensator, as demonstrated in Figure 3-3. Therefore, by adjusting V_q to zero, PLL aligns the voltage along the d-axis of the dq rotating frame with the phasor voltage V_{pcc} , so that in the steady-state V_d equals AC grid voltage magnitude.

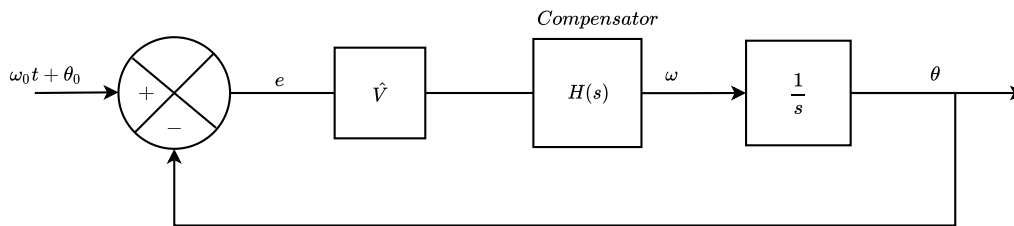


Figure 3-3: Control block diagram of the PLL

Power transfer via the VSC: is used to relate the AC input in the grid to the DC output in the DC-link capacitor. According to [51], the real and reactive power are controlled by the phase angle and the amplitude of the VSC line current with respect to the PLL voltage. In rotating frame of reference, the apparent power transfer S is the product of voltage V and

current i conjugate which can be expressed as:

$$\begin{aligned} S &= Vi^* = (V_d + jV_q)(i_d + ji_q)^*, \\ S &= (V_d i_d + V_q i_q) + j(V_q i_d - V_d i_q), \end{aligned} \quad (3-6)$$

where the active power P and reactive power Q are respectively given by

$$P = V_d i_d + V_q i_q, \quad (3-7)$$

$$Q = V_q i_d - V_d i_q. \quad (3-8)$$

Thus, the active and reactive power transfer, in per unit, via the VSC can be determined by (3-7) and (3-8) respectively. After involving the PLL in the VSC, the active and reactive power transfer equations are reduced to:

$$P = V_d i_d, \quad (3-9)$$

$$Q = -V_d i_q. \quad (3-10)$$

Therefore, the active and reactive control components of the current are utilized as a result of using the transformation into rotating dq coordinate. The active current component determines the contribution of the grid which supplies the required active power feed into the DC bus, while the reactive component determines the reactive power condition. Therefore, independent control of the active and reactive power can be achieved.

Line current control: the circuit diagram of the VSC, as seen in Figure 2-5, consists of grid voltage, voltage drop of line impedance and output DC voltage. Assuming constant grid voltage, the output voltage of active rectifier can be controlled indirectly by controlling the line current in the transmission line. As the AC voltage is already equal to V_d by PLL, from (3-9), it can be observed that the active power transfer is managed by controlling the d-axis current component whereas the reactive power transfer as per (3-10) by the q-axis current component. Thus, decoupled current control is involved to realize the objective of controlling active and reactive power transfer independently. The dq components of the DC-linked output voltage are expressed by rearranging (2-27) as :

$$\frac{V_{dc}}{2} \begin{bmatrix} d_d \\ d_q \end{bmatrix} = -L \frac{d}{dt} \begin{bmatrix} i_d \\ i_q \end{bmatrix} + \begin{bmatrix} -R & \omega L \\ -\omega L & -R \end{bmatrix} \begin{bmatrix} i_d \\ i_q \end{bmatrix} + \begin{bmatrix} V_d \\ V_q \end{bmatrix}. \quad (3-11)$$

This equation shows that the VSC has a multivariable dynamic. According to the basic relationship shown in Figure 3-4, the currents in d - and q -axes become perfect DC synchronized signals under balanced sinusoidal conditions with cross coupling terms $\omega L i_q$ and $\omega L i_d$ [52]. Thus, to eliminate the cross-coupling, the state variables of the grid current can be taken from (3-11) as:

$$\begin{bmatrix} u_d \\ u_q \end{bmatrix} = L \frac{d}{dt} \begin{bmatrix} i_d \\ i_q \end{bmatrix} + R \begin{bmatrix} i_d \\ i_q \end{bmatrix}. \quad (3-12)$$

Applying Laplace transform on (3-12), the system transfer function is determined as:

$$\hat{G}_i(s) = \frac{i_d}{u_d} = \frac{i_q}{u_q} = \frac{1}{R} \left(\frac{1}{1 + \tau s} \right). \quad (3-13)$$

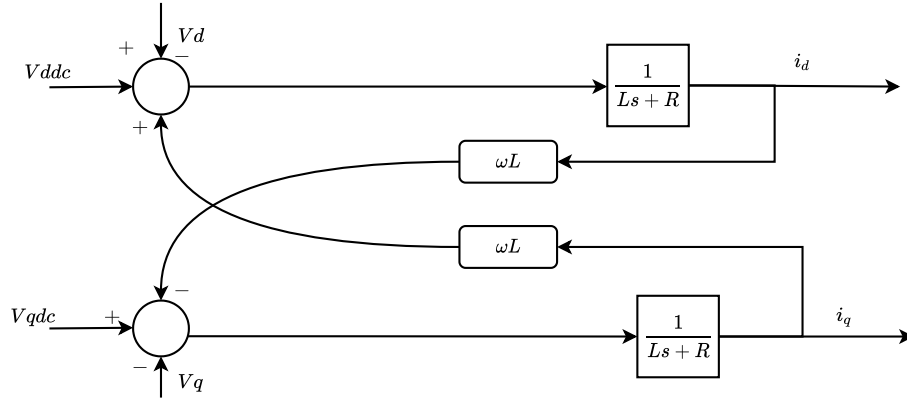


Figure 3-4: Multivariable dynamic model of a VSC system

Both current components have the same form of first order transfer function with time constant $\tau = L/R$, according to (3-13). The controller of each line current is structured using IMC principle and yields

$$F(s) = \frac{\alpha_i}{s} \hat{G}_i^{-1}(s) = \alpha_i L + \frac{\alpha_i R}{s}. \quad (3-14)$$

The current controller structurally looks Proportional Integral (PI) controller with a proportional gain k_{pi} given by $\alpha_i L$ and an integral constant k_{ii} determined by $\alpha_i R$. The controller bandwidth α_i is supposed to be a decade smaller than the switching frequency f_s as per [47] and estimated by

$$\alpha_i < \frac{2\pi f_s}{10}. \quad (3-15)$$

Considering the grid voltage as disturbance, the inner current control loop can be structured as shown in Figure 3-5. The converter is considered as an ideal power transformer with a time delay. The output voltage of the converter is assumed to follow a voltage reference signal with an average time delay equals half of a switching cycle, due to converter switches [52]. Hence, the general expression of the Pulse Width Modulation (PWM) converter is

$$Y(s) = \frac{1}{1 + T_a s}, \quad (3-16)$$

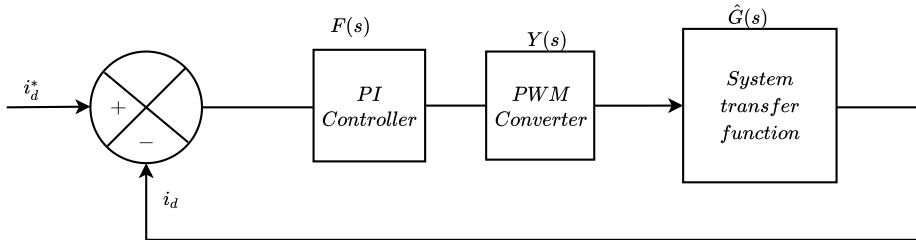


Figure 3-5: General block diagram of inner current control loop

where $T_a = T_{switches}/2$.

The series connection of the PI controller, the PWM converter, and the current transfer function form an open-loop transfer function denoted by $L_i(s)$. When the output of such connection feed backed, a closed-loop transfer function is formulated which can be denoted by $S_i(s)$. Both loops can be respectively determined by

$$L_i(s) = F(s)Y(s)\hat{G}_i(s) = \frac{\alpha_i}{s} \left(\frac{1}{1 + T_a s} \right), \quad (3-17)$$

$$S_i(s) = \frac{L_i(s)}{1 + L_i(s)} = \frac{\alpha_i}{T_a s^2 + s + \alpha_i}. \quad (3-18)$$

These explanations and expressions are applicable also for the q-axis current control loop. The duty ratio signals for switches in the a, b and c phases of the converter can be obtained by substituting (3-12) into (3-11) that yields

$$d_d = \frac{-u_d + \omega L i_q + V_d}{\frac{V_{dc}}{2}}, \quad (3-19)$$

$$d_q = \frac{-u_q - \omega L i_d + V_q}{\frac{V_{dc}}{2}}. \quad (3-20)$$

Taking into account the absence of zero-sequence component in a balanced system and through inverse Park's transformation, the duty ratio signals in a stationary abc frame of reference can be calculated as:

$$\begin{bmatrix} d_a \\ d_b \\ d_c \end{bmatrix} = T_{dq0/abc} \begin{bmatrix} d_d \\ d_q \\ 0 \end{bmatrix}. \quad (3-21)$$

A sinusoidal pulse width is modulated resulting in the variation of the average value of the low frequency waveform [19]. The duty cycle signals d_a , d_b , and d_c are compared in three separate comparators with a common fixed frequency saw-tooth shaped carrier wave as shown in Figure 3-6. Each comparator generates the firing signals for the corresponding Integrated Gate Bipolar Transistors (IGBT) switch. Therefore, it can be concluded that through Sinusoidal Pulse Width Modulation (SPWM), the average output voltage of the VSC of Figure 2-5 can be controlled.

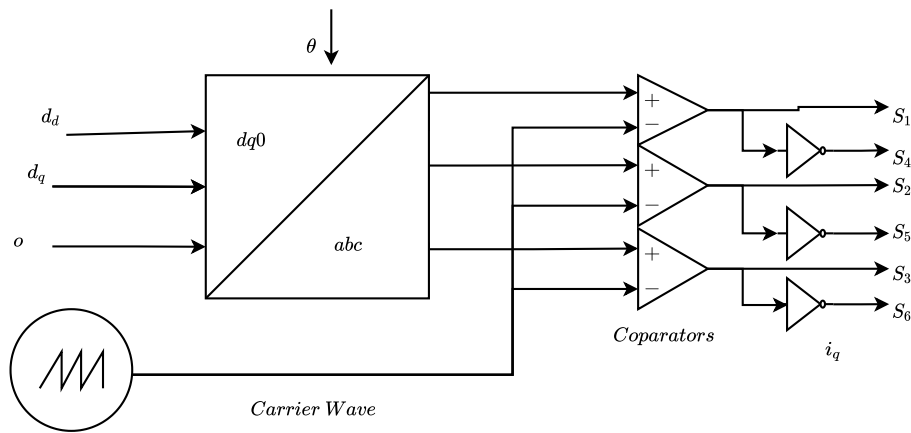


Figure 3-6: Sinusoidal pulse width modulation

Output voltage control: dimensioning of the DC-link voltage controller is determined by the transfer function between the current reference value to be given and the DC-link voltage [11]. The DC current in the output side of the VSC is the sum of current flow through the DC-capacitor and the load connected which can be expressed as :

$$i_{dc} = C \frac{dV_{dc}}{dt} + i_L. \quad (3-22)$$

The DC-link voltage is also equal to the voltage across the capacitor. Therefore, the instantaneous capacitor current can be expressed as a function of the DC link voltage as:

$$i_c = C \frac{dV_{dc}}{dt}. \quad (3-23)$$

From this expression, it can be seen that controlling the instantaneous current flowing into the DC link capacitor will lead to control of the DC link voltage. Applying Laplace transform on (3-23), the transfer function is written as:

$$\hat{G}_{dc}(s) = \frac{V_{dc}(s)}{i_c(s)} = \frac{1}{Cs}. \quad (3-24)$$

To obtain the controller structure for the DC voltage controller, the IMC approach is applied assuming a first order plant transfer function. Applying (3-24) to (3-3), the expression for the DC link voltage controller is

$$F(s) = \alpha_v C \approx k_{pv}, \quad (3-25)$$

where α_v is the controller bandwidth in rad/s , which is supposed to be a decade smaller than the inner current bandwidth in order to have cascaded control scheme. It can be observed from (3-25) that the controller has a proportional structure. In practice however, an integrator is included to ensure steady state error is eliminated. Therefore, the structure of the DC link voltage controller is a PI controller. The general diagram for the external controller is shown in Figure 3-7. Setting the capacitor current as the output of the PI controller, (3-23) can be rearranged as:

$$i_c = u_{dc} = C \frac{dV_{dc}}{dt} \quad (3-26)$$

$$u_{dc} = k_{pv}(V_{dc}^* - V_{dc}) + k_{iv} \int (V_{dc}^* - V_{dc}) \quad (3-27)$$

The active power exchange between the grid and DC-link voltage is realized by controlling the d-axis current component according to (3-9). In order to maintain the desired DC-link voltage, the inner current loop reference must be set by the outer voltage control loop such that the current reference is adequate for the capacitor and load requirements [49].

To obtain current reference along the capacitor, (2-28) is rearranged as :

$$u_{dc} = C \frac{dtV_{dc}}{dt} = \frac{1}{2}(d_d i_d + d_q i_q) \quad (3-28)$$

$$i_{dref1} = \frac{u_{dc} - \frac{1}{2}d_q i_q}{\frac{1}{2}d_d} \quad (3-29)$$

Applying PLL and assuming unity power factor, the d-axis current component lies inline with the AC voltage. Thus, the q-axis current component becomes zero and (3-29) is simplified to

$$i_{dref1} = \frac{u_{dc}}{\frac{1}{2}d_d}. \quad (3-30)$$

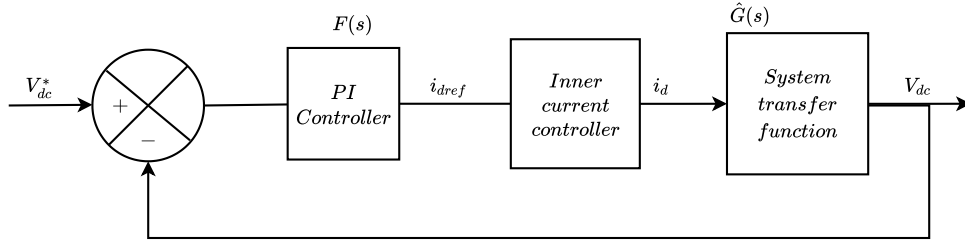


Figure 3-7: General block diagram of outer DC voltage control

Multiplying numerator and denominator by V_{dc} yields an equivalent expression described by

$$i_{dref1} = \frac{u_{dc}V_{dc}}{\frac{1}{2}d_d V_{dc}}. \quad (3-31)$$

According to [53], (3-31) holds in real operation of active front end converters where

$$\frac{1}{2}d_d V_{dc} \approx V_d. \quad (3-32)$$

Therefore, current set point for the DC-link capacitor current to maintain a desired DC-link voltage is calculated using

$$i_{dref1} = \frac{u_{dc}V_{dc}}{V_d}. \quad (3-33)$$

Under steady state the current flow through the capacitor becomes zero and as a result, the DC current flows through the load only. Therefore, active power balance relationship between the ac input and DC output after applying PLL given from (3-9) can be rewritten as:

$$P = V_d i_d = V_{dc} i_{dc} \quad (3-34)$$

Thus, the set point to compensate for the load current, can be calculated by rewriting (3-34) as :

$$I_{dref2} = \frac{V_d i_d}{V_{dc}} \quad (3-35)$$

The d-axis current reference is therefore the sum of the two reference set points.

The overall implementation in Simulink for the cascaded control structure is shown in 3-8, where the inner current is at least ten times faster than the outer voltage control design. Furthermore, the load current is feed forwarded for compensation.

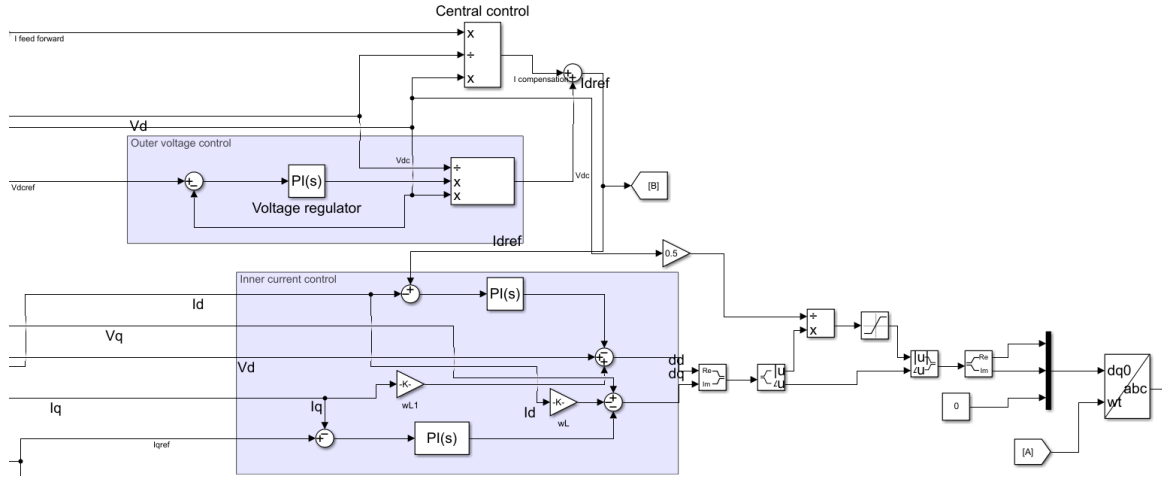


Figure 3-8: Implementation of cascaded control structure in Simulink

3-2-3 Control of Buck Converter

The hydrogen output as well as the total active power demand of the electrolyzer mainly depends on the amount of current flow through the stack. Therefore, these parameters of the electrolyzer can be controlled indirectly by proper current control design.

Neglecting the internal or parasitic resistances of components of buck converter of Figure 2-6, the current, that flows to the load, is regulated by adjusting the inductor current. Similar to rectifiers, applying IMC principle to input-to-output current transfer function of (2-37), the inductor current controller transfer function can be estimated as:

$$F(s) = \frac{\alpha}{s} G_{iL}^{-1}(s) = \alpha CR_L + \frac{\alpha}{s}. \quad (3-36)$$

This is equivalent to a PI controller with proportional gain $k_p = \alpha CR_L$ and integral gain $k_i = \alpha$. Thus, the generic structure of the load current controller is a PI controller. Combining the transfer functions and applying unity feedback yields the closed loop transfer function of the inner load current control loop described by

$$G_{cl}(s) = \frac{\alpha}{s + \alpha}, \quad (3-37)$$

where this equation has one pole at $s = -\alpha$.

3-3 Power-to-Hydrogen Conversion

The main function of an electrolysis system is to convert electrical energy into chemical energy (hydrogen). Thus, electrochemical models are the heart of any electrolysis system modeling work and enable to establish a relation between the input electrical power and the output hydrogen flow. From Faraday's law, the hydrogen production rate in an ideal electrolysis cell is proportional to the charge transfer flow, that is to the electric current I_c [34]. Assuming that the same current flows through every electrolyzer cell of the stack, the hydrogen molar

rate \dot{H}_2 production in mol/s can be expressed as:

$$\dot{H}_2 = N_c \frac{I_c}{zF}, \quad (3-38)$$

where N_c denotes the number of cells of the electrolyzer module. To calculate the stack hydrogen massive rate \dot{m}_{H_2} production in kg/s , (3-38) is modified to

$$\dot{m}_{H_2} = M_{H_2} \dot{H}_2, \quad (3-39)$$

where M_{H_2} is the hydrogen molar mass ($0.002 \text{ kg mol}^{-1}$). In order to take into account that all electrons are not involved into the electrolysis reaction due to leak current, parasitic reactions, etc. . . , thus, (3-39) can be extended by the multiplication of Faraday's efficiency η_f [54] as:

$$\dot{m}_{H_2} = \eta_f M_{H_2} N_c \frac{I_c}{zF}. \quad (3-40)$$

Faraday's efficiency η_f defines the fraction between the real generated quantity of hydrogen H_2 and the theoretical hydrogen quantity which could be produced according to the electrical energy input [40]. The Faraday's efficiency lower than 1 is caused by the parasitic current that appears in the real electrolysis process and that does not contribute to the generation of useful hydrogen. Part of the parasitic current flows between the cells either without taking part in the oxidation and reduction half-reactions or participating in non-desired electrochemical reactions. The rest of the parasitic current generates hydrogen, but that is lost by crossover the diaphragm of the cells. According to [34], when the electrolyzer operates at its rated production conditions, it obtains maximum Faraday's efficiency of 95%.

The overall stack efficiency η_s can be estimated by taking the ratio of the output power produced in the form of hydrogen P_{H_2} to the electrical power P_{elec} consumed by the electrolyzer, which is expressed as:

$$\eta_s = \frac{P_{H_2}}{P_{elec}}. \quad (3-41)$$

Where P_{H_2} is the product of produced molar hydrogen and its instant heating value H_{H_2} , at the same time, P_{elec} is calculated by multiplying the input current I_c and stack voltage V_s of the electrolyzer [5]. Taking this concept and (3-40) into consideration, Eq. (3-41) is rewritten as:

$$\eta_s = \frac{\dot{m}_{H_2} H_{H_2}}{I_c V_s} = \frac{\eta_f M_{H_2} N_c I_c H_{H_2}}{I_c N_c V_c zF}, \quad (3-42)$$

$$\eta_s = \frac{0.95 M_{H_2} H_{H_2}}{2FV_c}. \quad (3-43)$$

The stack efficiency, as can be observed from Eq. (3-43), is directly proportional to the hydrogen heat value H_{H_2} , but inversely proportional to the cell voltage FV_c . The hydrogen heat value is the energy content of hydrogen, given by the lower combustion value ($120.86 * 10^6 \text{ J/kg}$), which is released during combustion. Considering the electrolyzer has constant cell voltage (e.g., $V_c = 1.6 \text{ V}$) at its operational range, the PEM stack efficiency reaches up to 73%. Assuming constant Faraday's efficiency, it can be observed from (3-40) that the only parameter that affects the hydrogen production is the input current I_c . The hydrogen output is directly proportional to the current fed to the electrolysis stack. Therefore, in order to

control the hydrogen generation output, which is the primary function of the power-to-gas plant, the current to the stack must be precisely controlled. In addition, the stack current is directly related to the active power demand of the electrolyzer.

The main purpose of the aforementioned power converters (rectifier and buck converter) is to regulate the power demand of the hydrogen production. Thus, the electrolyzer is connected to the power converters by replacing the resistive load of the DC-DC converter in Figure 2-6 with a series connection of a parasitic resistor R and a controlled voltage source, as the electrolyzer provides a stack voltage V_{ely} for a given current input i_{ely} [55]. The overall connection of electrolyzer with power converters is shown in Figure 3-9, where the rectifier determines the input DC voltage of the buck converter from AC grid. The current flow to the electrolyzer is measured to be compared with the reference current which is calculated by the higher level controller based on the market, grid condition or alarm. The error is regulated by a PI controller to have the desired duty ratio that is to be compared with sawtooth wave of a constant frequency. Finally, the PWM controls the switch of the buck converter to optimize the current flow to electrolyzer based on its hydrogen demand.

The Implementation of the electrochemical model in this research is based on [39] with an experimental validation of a 36 kW PEM electrolyzer.

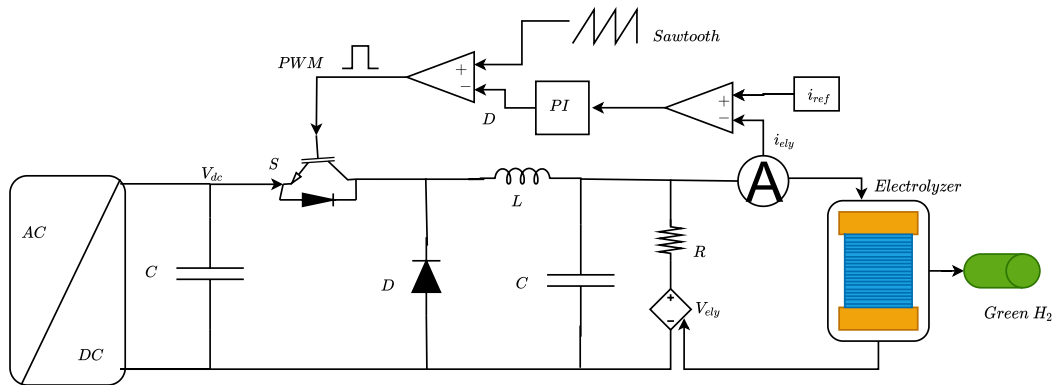


Figure 3-9: Electrolyzer connection with power converters

Model Application for Grid-Support

The transition of power system from traditional fossil fuel based to renewable resources based modern distributed generation enables reduction of greenhouse gases (specially CO₂) emission as well as energy dependency of a nation. On the other hand, distributed energy resources increase the complexity of the power system due to their power electronics based interface to the power network that effects lower inertial response. The consequence is that in the case of disturbances and supply/demand imbalances, the inertia that slows down the natural reaction of the system and buys the controllers and the operator time to take actions is significantly reduced [6]. As a result, the rate of change of frequency (RoCoF) is much higher, as can be observed in Figure 4-1, in such systems which may cause load shedding. By contrast, the faster dynamic response of power converters compared to conventional controllers, as shown in Figure 4-1, could create unforeseen control approach to compensate the low inertia response of distributed generation systems [56].

One of the promising power electronics interfaced loads for grid stability is the Proton Exchange Membrane (PEM) electrolyzer. It can be interfaced to AC grid through two topologies of AC power converters based on its influence for grid parameters [50]. The first is a grid-feeding power converter which enables the PEM electrolyzer to follow the voltage amplitude and frequency references of the AC grid. Such structure of power converter does not allow for the electrolyzer to participate in case the power network is exposed to disturbances or power imbalances. And the second is a grid-support power converter that contributes the regulation of the AC voltage and frequency of the grid by controlling the active and reactive power deviations respectively. Both converter structures are demonstrated in Figure 4-2. A Voltage Source Converter (VSC), in grid-supporting mode, is implemented in this study by applying higher level controller to analyze the role of PEM electrolyzers in ancillary services.

The ancillary service definition differs based on its role for power systems from nation to nation. According to European Commission, ancillary services are stated as all services necessary for the proper operation of the transmission and distribution networks of the power system [49]. There are several classifications of ancillary services, but this research is limited to: Frequency Containment Reserve (FCR), Automatic Frequency Restoration Reserve (aFRR), and voltage control service. The first two are related to levels of frequency control to optimize

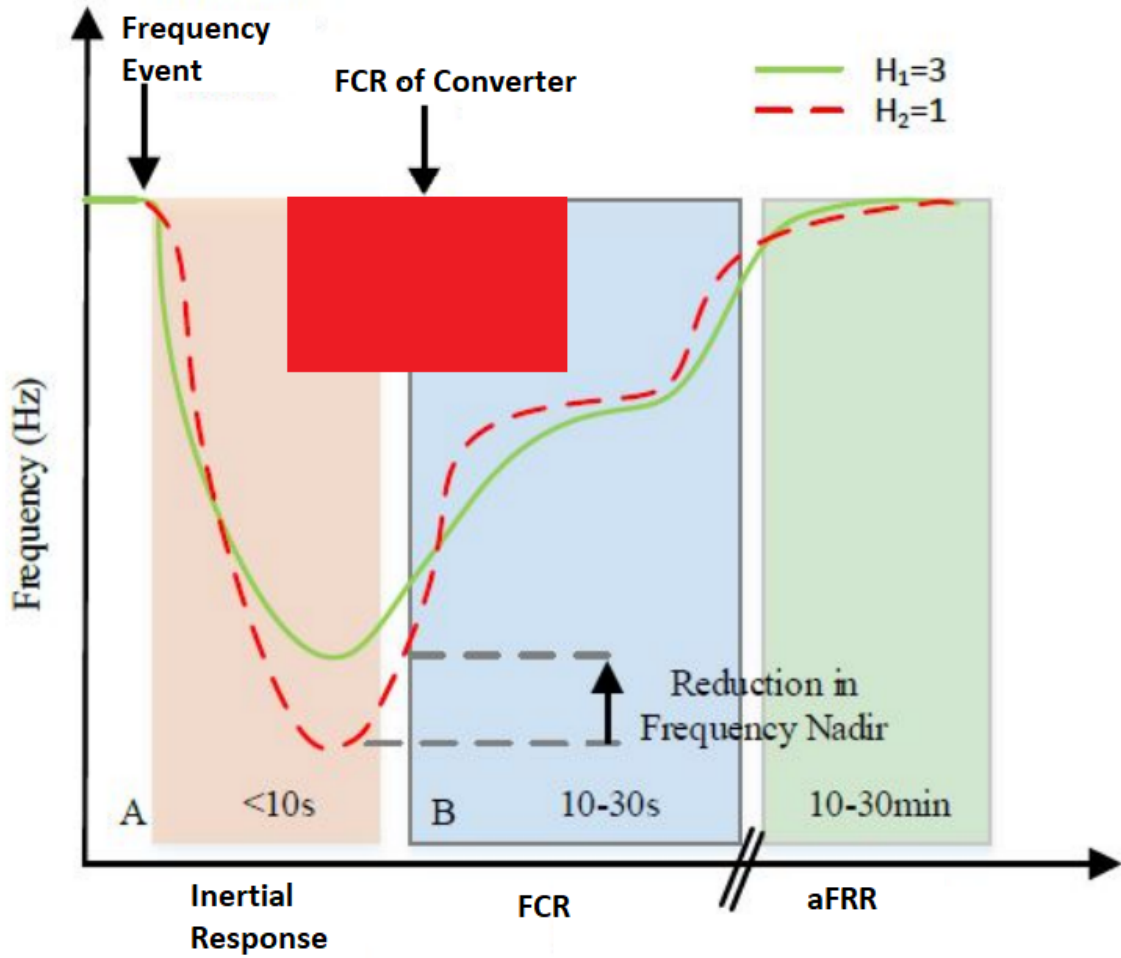


Figure 4-1: Multiple time-frame frequency response in a power system following a frequency event: adapted from [6]

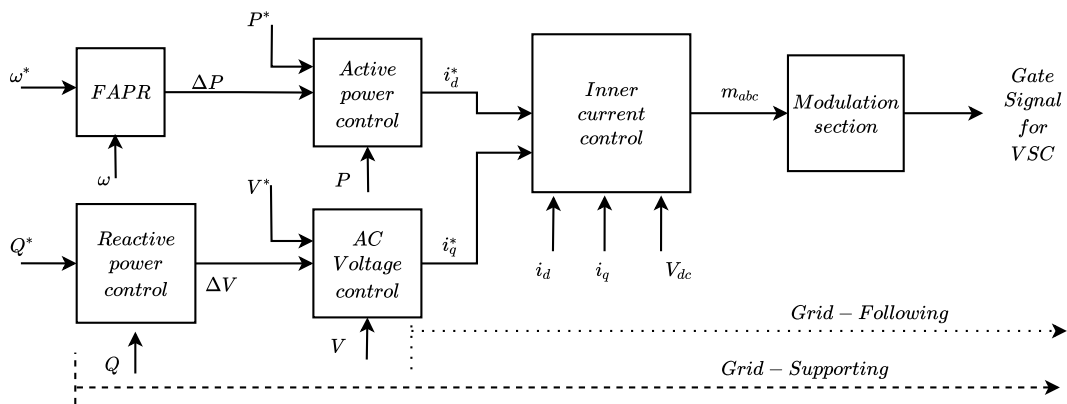


Figure 4-2: Power converter topologies for interfacing PEM electrolyzer with a power system

active power system stability as shown Figure 4-1, whereas the voltage control is applied to compensate any reactive power deviation. The main goal of the preceding subsections are to ascertain the effectiveness of PEM electrolyzers for the provision of the aforementioned ancillary services.

4-1 PEM Electrolyzer as FCR

When the frequency variation of a power system reaches the emergency condition, the FCR (formerly called primary frequency control) is activated by an automatic governor control. In addition, the FCR is provided specifically to control system frequency variations and provides the first response to frequency deviations that follows loss of supply.

In developing a dynamic model of a PEM electrolyzer for frequency response analysis, the two key points to be considered are: the simulation time horizon which is from milliseconds to several seconds, and the time-step which must be small enough to capture fast frequency transients. These points are critical especially under low-inertia conditions with high RoCoF that can cause load shedding.

As the electrolyzer's thermal sub-model has a time constant in the order of hours [57], therefore, it is legitimate to ignore the thermal sub-model dynamics by assuming a constant operating pressure and temperature of PEM stack. In addition, there is no feedback signal from the H₂ production sub-model to either the electrical or thermal parts. Furthermore, Balance of Plant (BoP) components are fed from a separate AC supply as shown in Figure 2-13 and are modeled by a constant load, as it can be assumed that most of them have a fixed power consumption as briefly explained in Section 2-4. The proposed model of the stack for frequency response analysis can therefore be represented by its electrochemical model, as shown in Figure 2-11, which has usually a reaction time under one second and is much faster than generator governors.

To optimize the electrolyzer to support the objectives of ancillary services provision, an additional control system is required. The front-end controller is this control system and communicates with low-level controls to form a hierarchical controller with extended capabilities, such as the capability to simultaneously respond to market price signals, the condition of Transmission System Operators (TSO) and internal signals such as electrolysis process alarms [8], as shown in Figure 4-3. However, the higher level control in this case is limited to stabilize frequency change in power system.

An advanced Fast Active Power Regulator (FAPR) in series with an active power Proportional Integral (PI) controller, as shown in Figure 4-2, is used for fast active power-frequency control to quickly and effectively adjust the active power at the AC side of the VSC, which is used to interact the renewable energy-based generation system with the electrolyzer. According to the comparison among different forms of FAPR in [7], a droop based approach is the simplest and most common frequency tracking method, as such implemented in this study.

The frequency f of the network is measured at the Point of Common Coupling (PCC) of the PEM electrolyzer using Phasor Measurement Unit (PMU) and compared with 50 Hz grid reference frequency as seen in Figure 4-3. The frequency error is then passed through a 10 mHz deadband for selective operation of the controller by avoiding unnecessary activation of the FAPR controller.

Further, the frequency error is amplified using a proportional gain k_d which is the ratio of active power deviation ΔP to the frequency change Δf . The output ΔP of the frequency

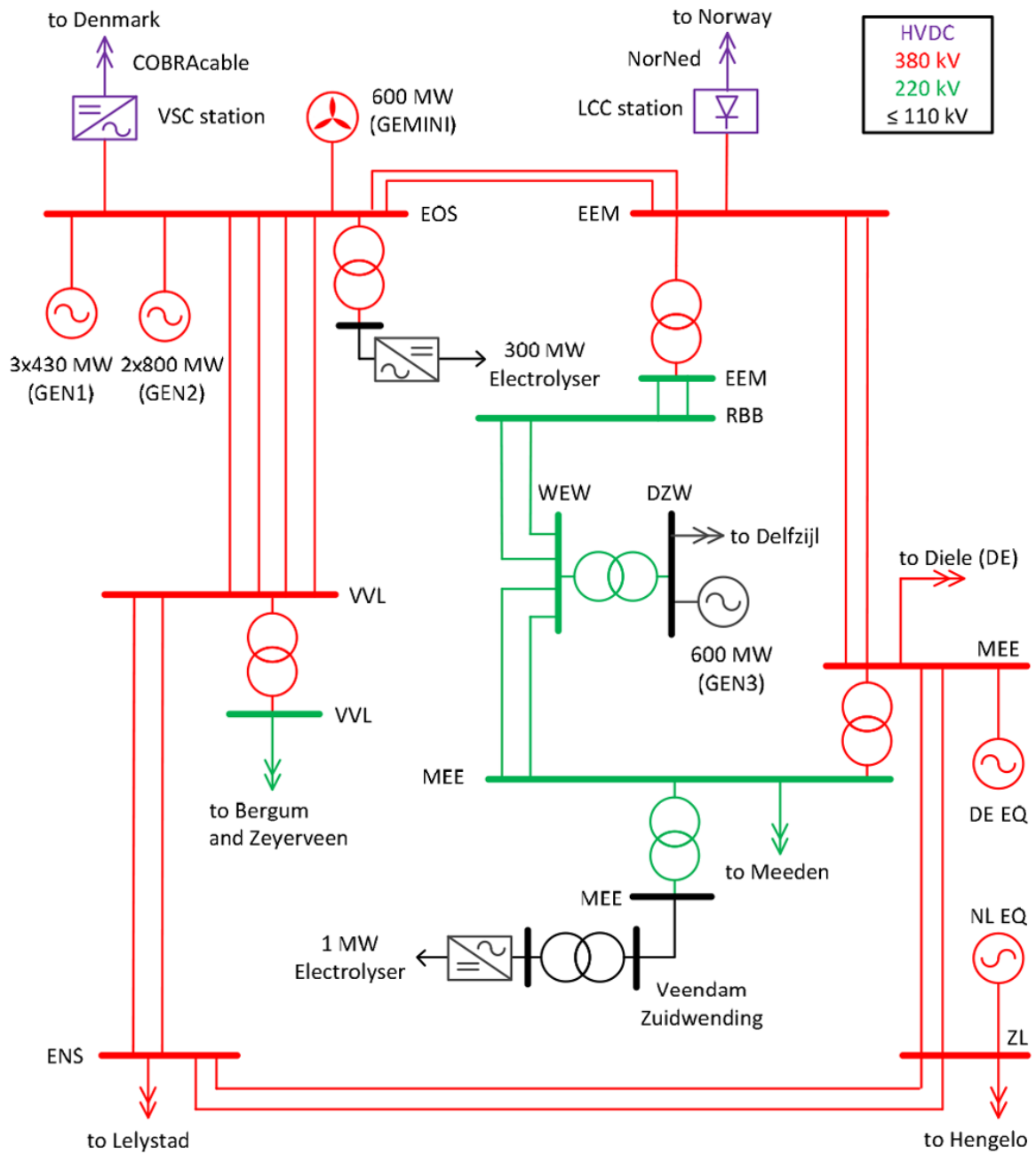


Figure 4-4: Considered network topologies for grid-supporting electrolyzer study: Extracted from [7]

In the first case, the active power at EON substation is reduced by 200 MW due to slow wind speed at the GEMINI wind farm. To study the impact of the electrolyzer, its participation as FCR is varied from 0 to 100% by replacing the primary frequency support of some generators with FCR support by the electrolyzer.

From the simulation result shown in Figure 4-5, it can be seen that the replacement of FCR support by the electrolyzer has a positive effect on the frequency response of the system, as the electrolyzer has the ability to react faster to deviations of the frequency compared to the governor response of generators. Furthermore, it can be observed that the higher percent usage of electrolyzer as FCR, the better improvement in RoCoF and nadir frequency.

In the second study case, the loss of load demand by 200 MW at MEE substation is considered. First, the electrolyzer operational set point has been reduced to 190 MW, to enable upwards regulation of the electrolyzer consumption and apply 37% of electrolyzer for FCR support. The simulation result, as seen in Figure 4-6, indicates that the electrolyzer has a positive effect on the grid frequency stability, as the electrolyzer responds faster for any frequency deviation.

It can be concluded that electrolyzers have a positive effect on frequency stability after losing generation capacity or load, as electrolyzers are able to respond faster to frequency deviations than the governor control of conventional generators.

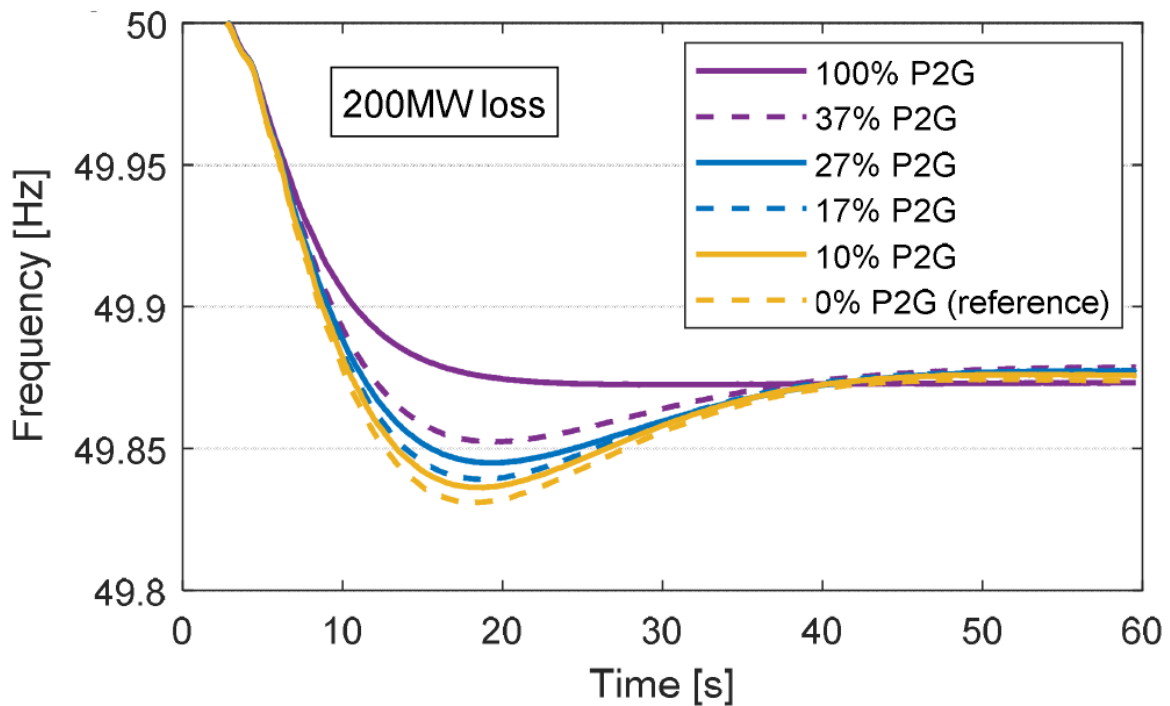


Figure 4-5: Frequency response of the system with different shares of electrolyzer FCR capacity for a loss of 200 MW generation capacity: Extracted from [8]

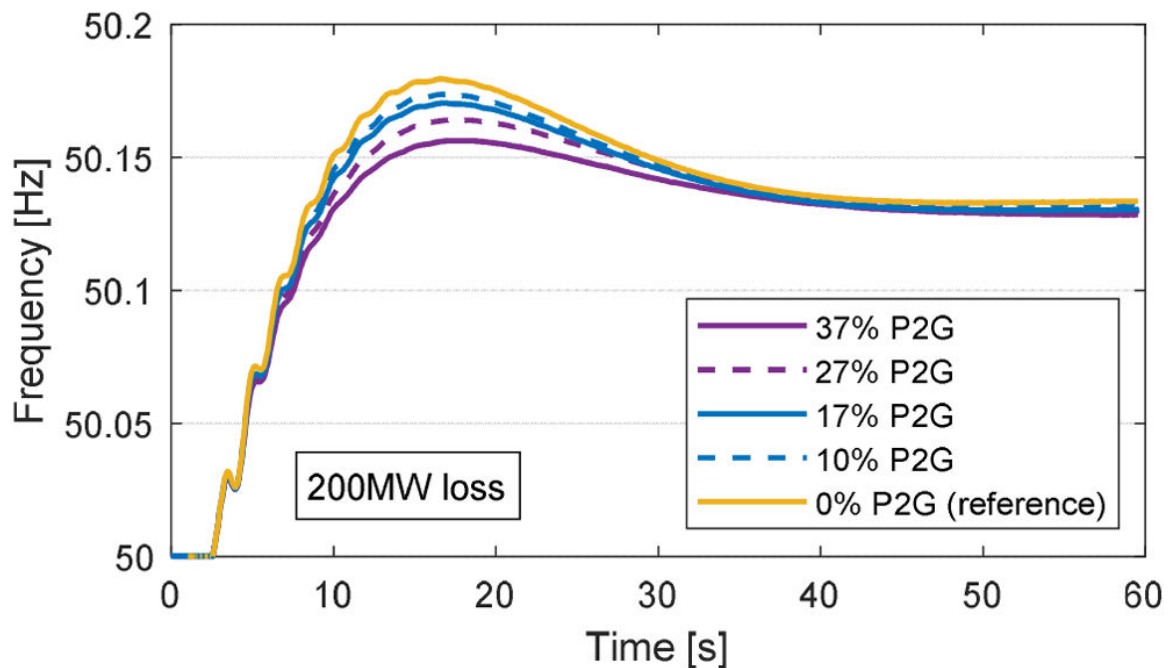


Figure 4-6: Frequency response of the system with different shares of electrolyser FCR capacity for a loss of 200 MW load demand: Extracted from [8]

4-2 PEM Electrolyzer for aFRR

The aFRR, formerly known as secondary frequency control, is the restoration process to bring the frequency back to the nominal value using Automatic Generation Control (AGC).

The electrolyzers' operating point adjustment can be utilized to offset short-term variations in demand that might affect the stability of the power system. The reaction time of the electrolyzer for set point changes is less than 1 second, and the set point can be maintained for unlimited amounts of time, so that the electrolyzer can act as aFRR. In addition, for aFRR, fuel cells could take advantage of the cheap hydrogen supplied by electrolyzers to place voluntary bids for upward regulation during periods with high settlement prices [12].

4-3 Voltage Amplitude Regulation

Voltage control service is a service aimed at ensuring the terminals of all equipment in the power system operate within acceptable voltage limits using network arrangements. In addition, it has the objective to minimize the reactive power flow to reduce the power losses in transmission line [3]. In power system theory, these objectives are achieved by various methods of voltage control such as automatic voltage controller, passive compensation, and active compensation. However, this section discovers the potential of the PEM electrolyzer for voltage amplitude regulation at the PCC.

The same as discussed for the active power regulation, a control strategy can be adopted for the reactive power regulation by electrolyzer as well. As can be observed in (3-10), the

reactive power injected to the PEM electrolyzer mainly depends on the q-axis current i_q . The reactive power Q of the network is measured at the PCC of the PEM electrolyzer using PMU and compared with Q_{ref} grid reference reactive power as shown in Figure 4-3. The reactive error is then passed through a deadband for selective operation of the controller by avoiding unnecessary activation. Furthermore, the reactive power error is amplified using a proportional gain k_q which is the ratio of the voltage change ΔV to the reactive power deviation ΔQ . The output ΔV of the voltage tracking is added as an auxiliary reference signal to determine the reference grid voltage.

In addition, the measured grid voltage at the PCC is compared with the new reference voltage to be controlled by the outer voltage PI controller which determines the reference signal i_{qref} of the inner current controller of the VSC. It can, thus, be concluded that the response of the electrolyser to voltage amplitude deviation is determined by its VSC and its controllers. Literature [58] studies the interaction of 500 kW electrolyzer, 625 kW rectifier and 2 MVA wind turbine generator to regulate the voltage fluctuation at the point of common coupling. Fluctuations in active and reactive output power of the wind turbine connected to a weak grid will typically cause voltage fluctuations, therefore reducing the power quality in the grid. The 25% larger converter capacity comes at a low cost and is used for reactive power compensation by serving as a static synchronous compensator (STATCOM). The paper demonstrates that the voltage quality is improved, by flexible operating capabilities of the electrolyzer, without extra losses.

Simulation Results and Discussions

This chapter provides an overview and analysis of the response of the Proton Exchange Membrane (PEM) electrolyzer model using MATLAB and Simulink. The performance of the model is tested with a simple network comprising a voltage source, a medium voltage transmission line, a transformer, and an electrolyzer. The network is adequate for analyzing the response of the model to set point changes driven by power system disturbances, local basic commands, and also for analyzing the feasibility of ancillary services.

The tests were demonstrated using the Simulink diagram shown in Figure 5-1 that consists of a 600 V voltage source, which represents the infinite grid, connected to a reactive load, a resistive load, and via a step-down transformer and power electronics interfaced to the electrolyzer. The nonlinear model of the PEM electrolyzer implemented in the test is a stack, taken from the study of [39], that comprises 60 series connected cells consuming 46 kW power. Because in this example the connection to power electronics is crucial, also the electric dynamic behavior should be modeled [55].

The electrolyzer's rectifier is modeled with an average mode. The average model performs as a three-phase, two level, Pulse Width Modulation (PWM) converter, except that switching frequency phenomena are averaged over the switching period. The principle is to make a continuous model that averaged over one switching period has the same terminal voltage-current relationship as a full, switched, model. The model makes it possible to run simulation with much larger time step, resulting therefore a much faster and larger time span simulations. The test case to analyze the response of the PEM electrolyzer consists of two categories. The first test covers the responses to basic step commands, and the second test simulates the response to the power system disturbances such as a typical three-phase fault and power imbalances.

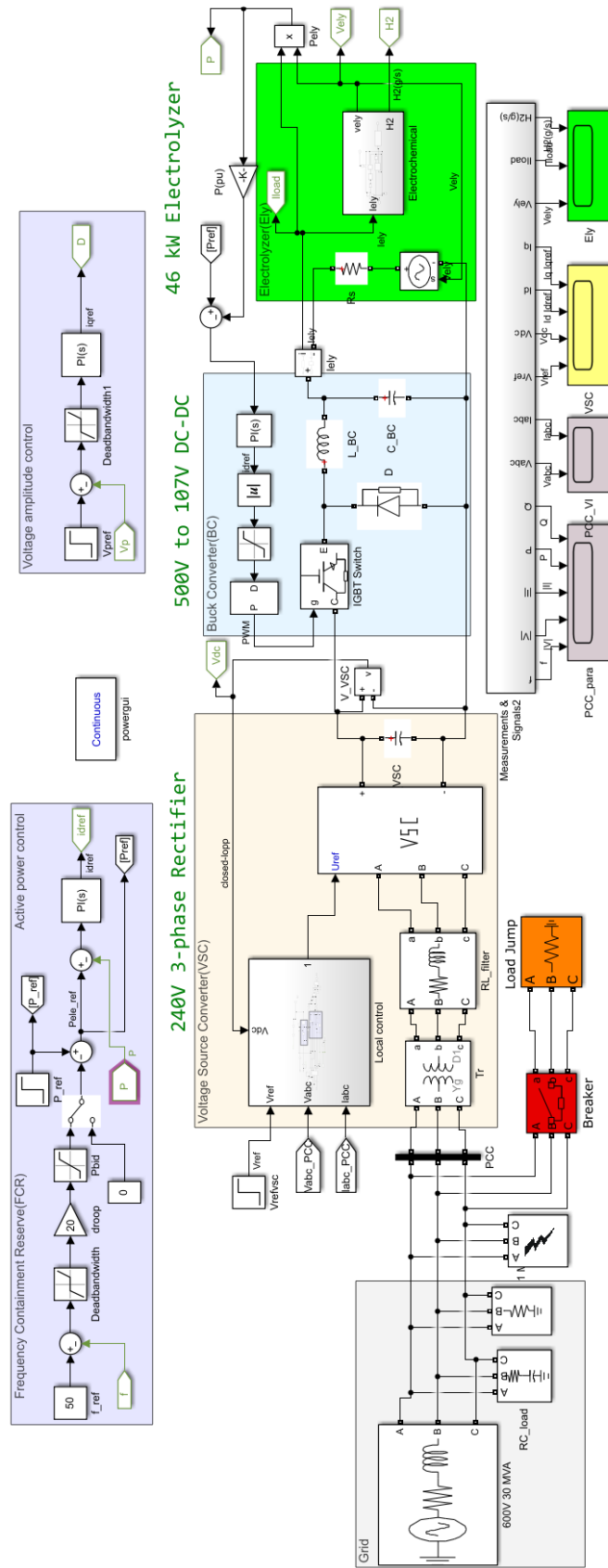


Figure 5-1: The electrolyzer model in Runtime module of Simulink

5-1 Response to Step Changes

This section demonstrates the response of the PEM electrolyzer for a step change (increase/decrease) in reference voltage of the Voltage Source Converter (VSC), power demand of the PEM stack as well as grid voltage.

Test 1: Step change in VSC voltage: as stated in section 2-2-1, the output voltage of the VSC can vary based on the wind speed in case the electrolyzer is connected to a wind turbine. Therefore, the reference voltage $V_{ref-vsc}$ of the rectifier represented by step input is altered by the front end controller based on the wind condition. A 20% increase and decrease in the step input impact a respective enhancement and reduction with the same percentage in the DC input voltage V_{in-ely} of electrolyzer as shown in Figures 5-2 and 5-3 respectively. In both cases, the signals settle within milliseconds after certain overshoots.

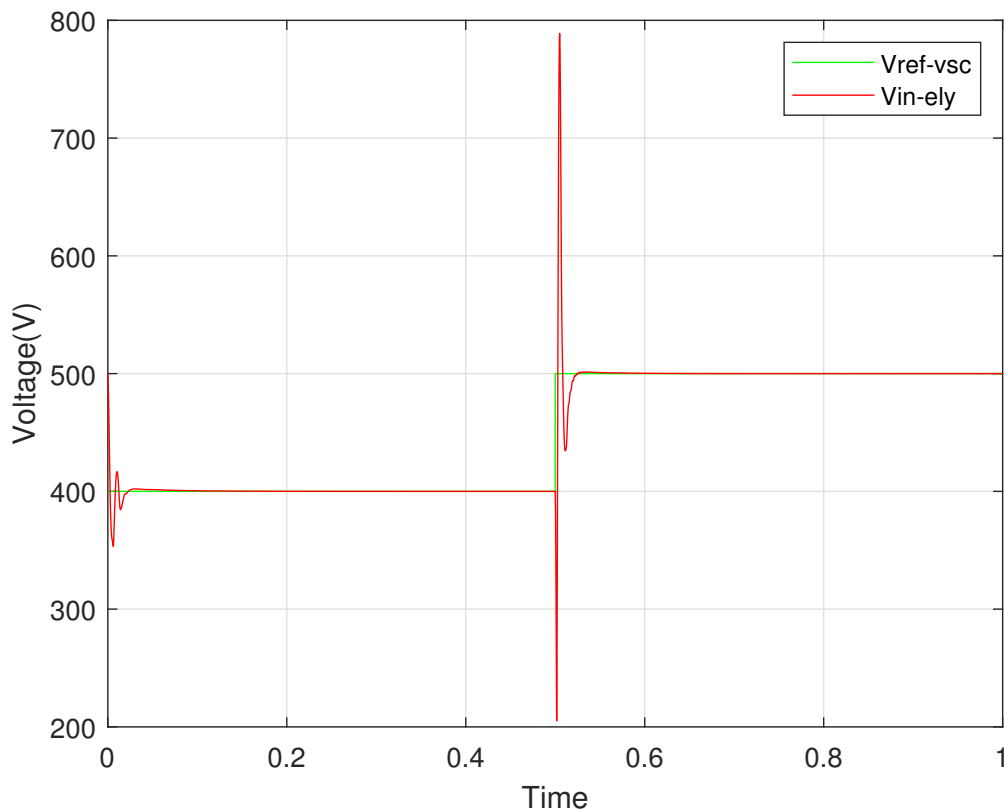


Figure 5-2: Response of the electrolyzer model to VSC voltage set point increase

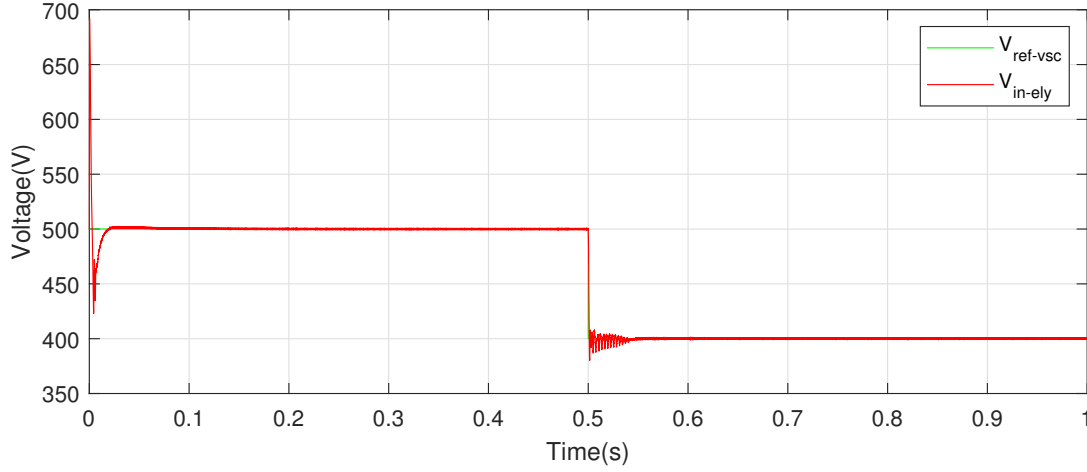


Figure 5-3: Response of the electrolyzer model to VSC voltage set point decrease

Test 2: Step change in electrolyzer active power: the active power drawn to the electrolyzer can be commanded by an external sources such as a central dispatch center, hydrogen market or local alarms. The central dispatch center in the model represents the signal from Transmission System Operators (TSO) who enables secondary or tertiary frequency control capabilities of the PEM electrolyzer, whereas the hydrogen market tracks the price by comparing to its reference. Furthermore, the local alarms detect the current operating condition of Balance of Plant (BoP) of the electrolyzer. These set-points adjust the active power demand of the stack and further translated by the front end controller into signals for the low level controllers. This is the basic operating principle used to store excess generated energy as hydrogen gas. Figures 5-4 and 5-5 show the Simulink model's response with negligible overshoots for the stack active power P_{ref} step up and down by 30% respectively. It can be observed from both Figures that the hydrogen H_2 gas delivered by the PEM electrolyzer has similar ramp rate as the power demand. This result is obtained by adjusting the current flow, to the electrolyzer via the switch of the buck converter, with a Proportional Integral (PI) controller as shown in Figure 5-1. The model is capable of emulating the response of an electrolyzer whose stack power set-point has been adjusted upward and downward via a step command.

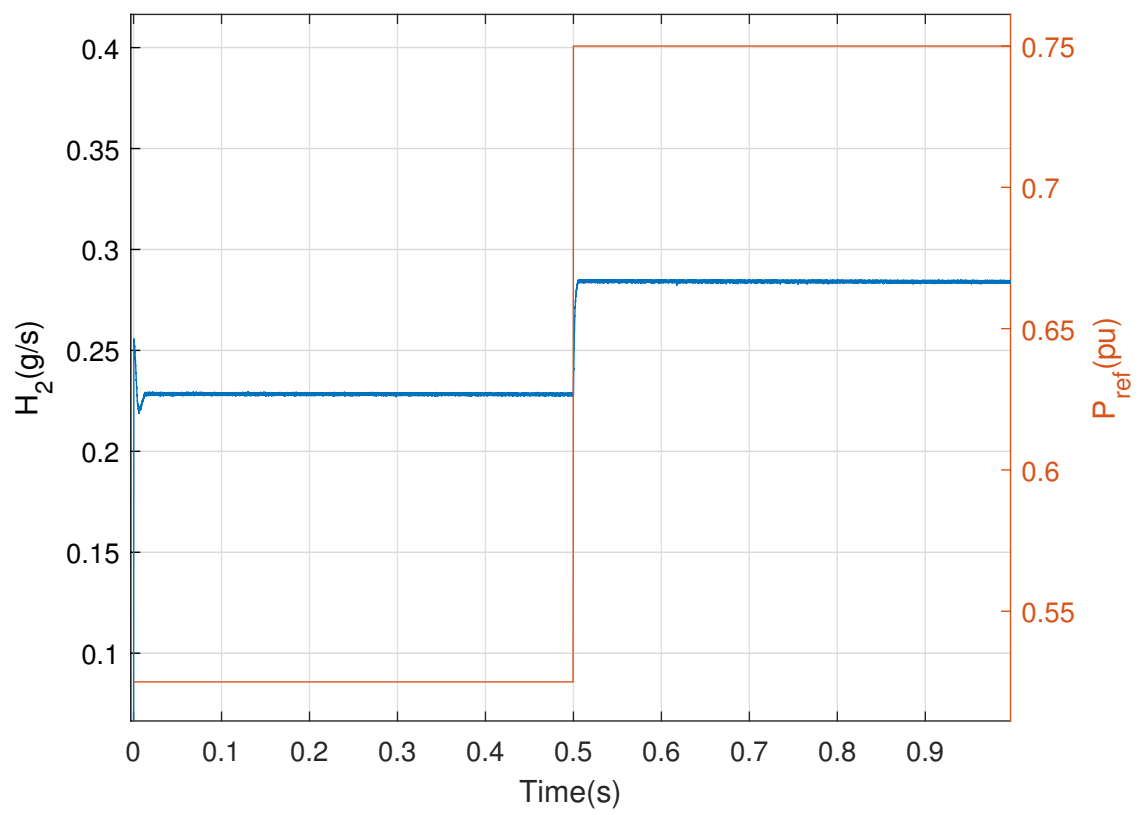


Figure 5-4: Response to the active power step up command

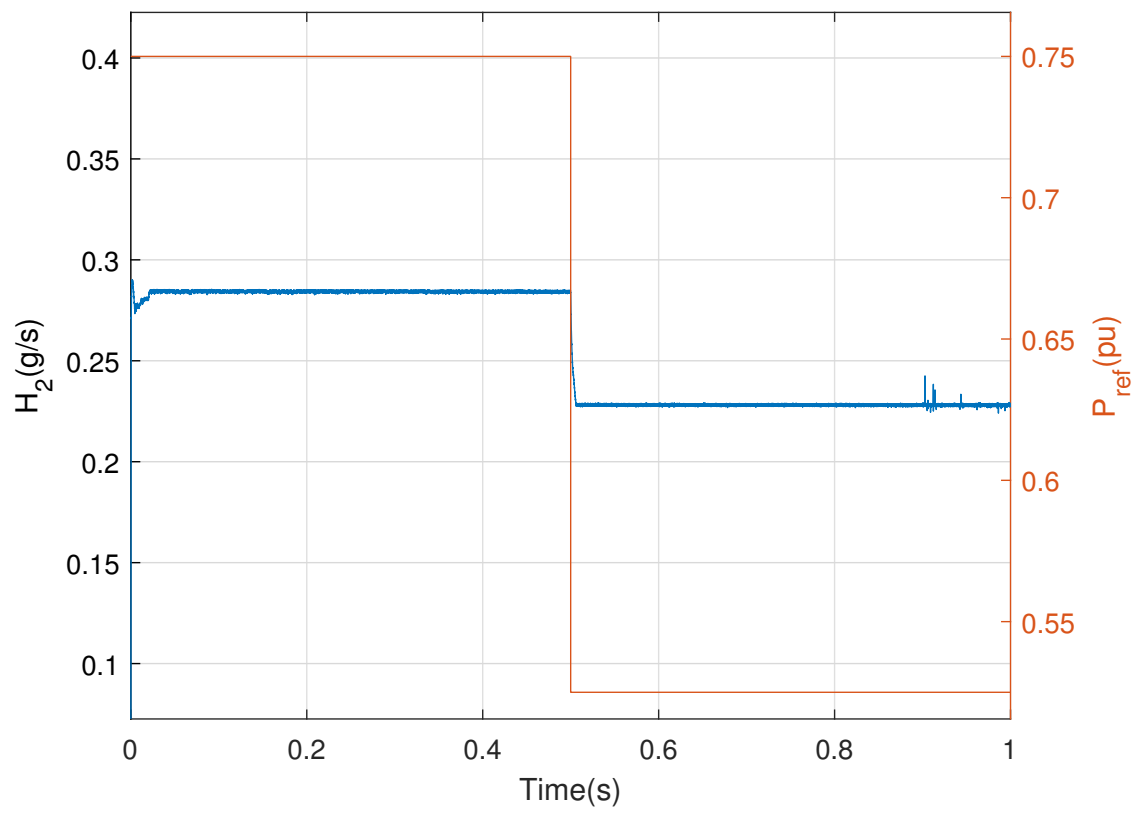


Figure 5-5: Response to the active power step down command

Test 3: Step change in a grid voltage: voltage control service aims at ensuring a power system to operate within acceptable voltage limits using network arrangements and reactive power compensation. PEM electrolyzers can also be applied for the regulation of the grid voltage to keep within its operating range. The converter control can inject or absorb reactive power in addition to its capability to adjust active power. The reference voltage depends on the reactive power deviation which is adjusted by a higher level controller based on the grid operator command. This voltage is compared with a measured voltage at the Point of Common Coupling (PCC) to be tuned by a PI controller, and determines the q-axis reference current i_{qref} of the inner controller as shown in Figure 5-1. The impacts of the 10% step changes, in reference voltage after 0.5 s, are shown in Figures 5-6 and 5-7 that can be observed a respective increase and decrease in the measured voltage V_{pcc} at the PCC. In addition, these changes mainly affect the reactive power Q_{ely} rather than the active power P_{ely} of the PEM electrolyzer which indicates independent control of the apparent power components.

From the above three tests, it can be observed that the stack responds very fast and settles down within milliseconds after the application of step changes. For instance, the model's simulation takes almost 120 ms settling time for the step-down in the VSC voltage set point as shown in Figure 5-3. Similarly, according to literature [59], the system-level response time for the real PEM electrolyzer ramping down occurs quickly and is nearly complete after 140 ms. Thus, comparing the response profile and settling time of the model to that for the real electrolyzer, it can be concluded that the generic model replicates the real system fairly in the same order of response time. Moreover, this feature is particularly of interest for the application of the PEM electrolyzer in the ancillary services of power systems, as covered in chapter 4, since electrolyzers are known to have relatively faster response than generator governors which have a response time in the order of tens of seconds as shown in Figure 4-2.

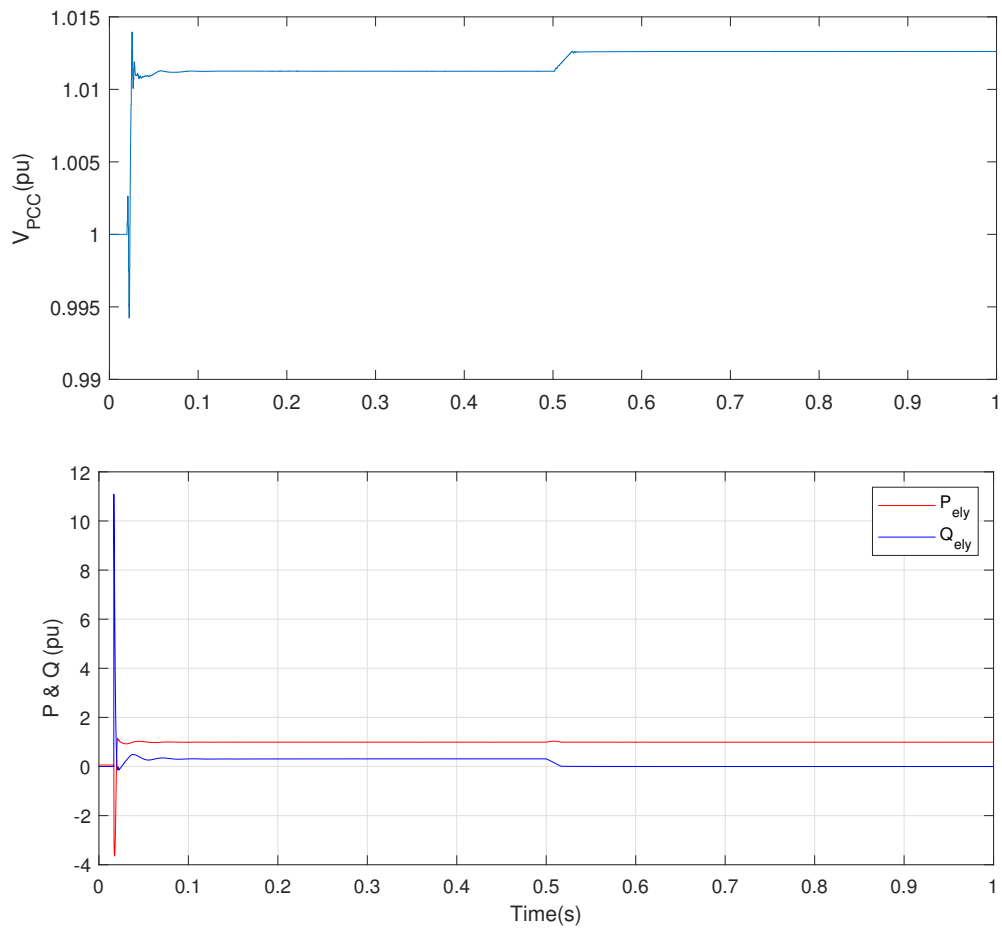


Figure 5-6: Simulation result to a step-up in grid voltage set point

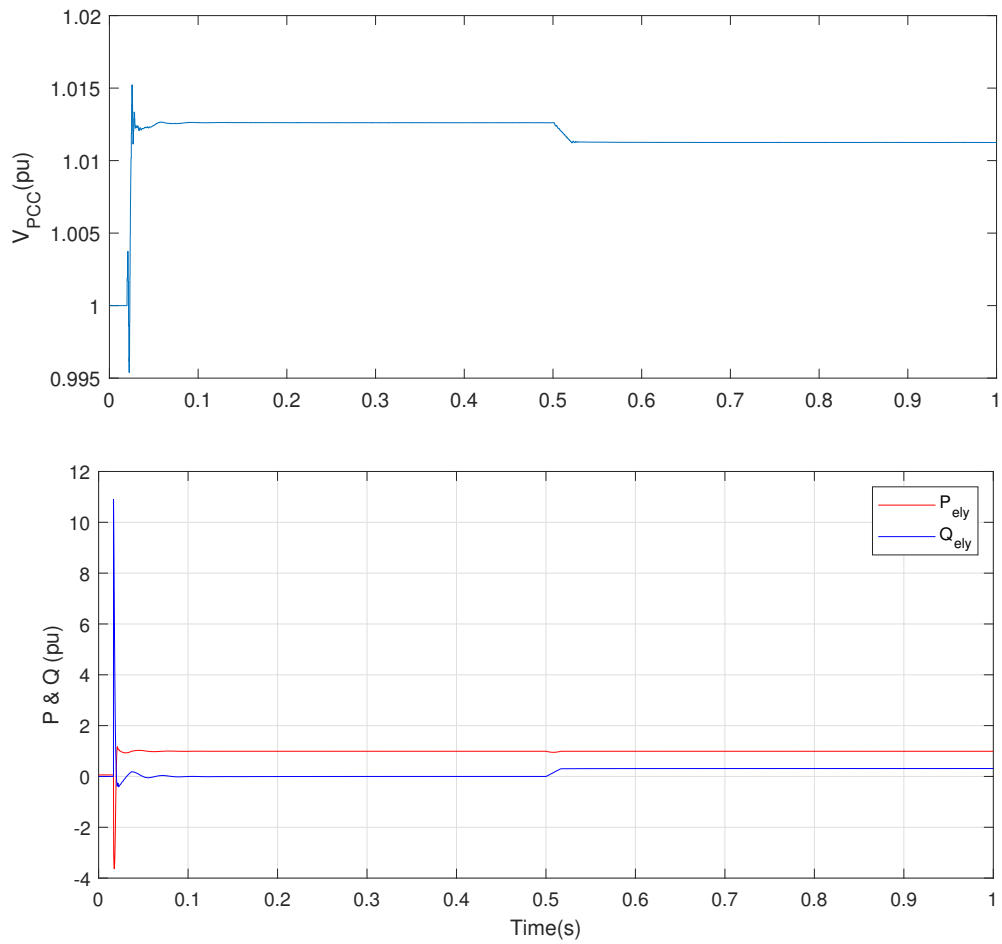


Figure 5-7: Simulation result to a step-down in grid voltage set point

5-2 Response to Power System Disturbances

The occurrence of a fault or a power imbalance in system network can act as disturbances. The fault can be defined as the failure of insulation partially or completely that interrupts the normal flow of current in the power system. The fault on the transmission lines mostly occurs due to lightening at which the insulation flash over occurs. The high voltage between the conductors and the grounded tower causes ionization, which creates a path to ground for the charge induced by the lightening [60]. The low impedance path to ground allows flow of current from the conductor through the ground, and back to the neutral of the transformer or generator. Faults occurring in transmission line can be either asymmetrical, that consists of line to ground faults and line to line faults, or symmetrical that corresponds to three-phase faults. In this section however, a simulation result is only given for a symmetrical fault, because this type of fault is the most severe in terms of potential damage to power system components. On the other hand, an active power imbalance in power system occurs due to a difference between the generated power and power demand. The impact of both the three-phase fault and power imbalance are demonstrated in the preceding tests.

Test 4: Response to a three-phase fault: during a 5 ms fault period, the high active power difference between generation and consumption leads to large frequency drop of the grid which is cleared with in 30 ms by the fast response of PEM electrolyzer as shown in Figure 5-8. Furthermore, the low impedance path to the ground during fault allows high flow of current i_{pcc} and low voltage V_{pcc} in the point of common coupling of electrolyzer as shown in Figure 5-8. It can be observed that the controller enables to recover the bus voltage back to its pre-disturbance level within 0.1 s. This indicates a significant improvement in the recovery time compared to governor controller, albeit with some overshoot specially in the current signal.

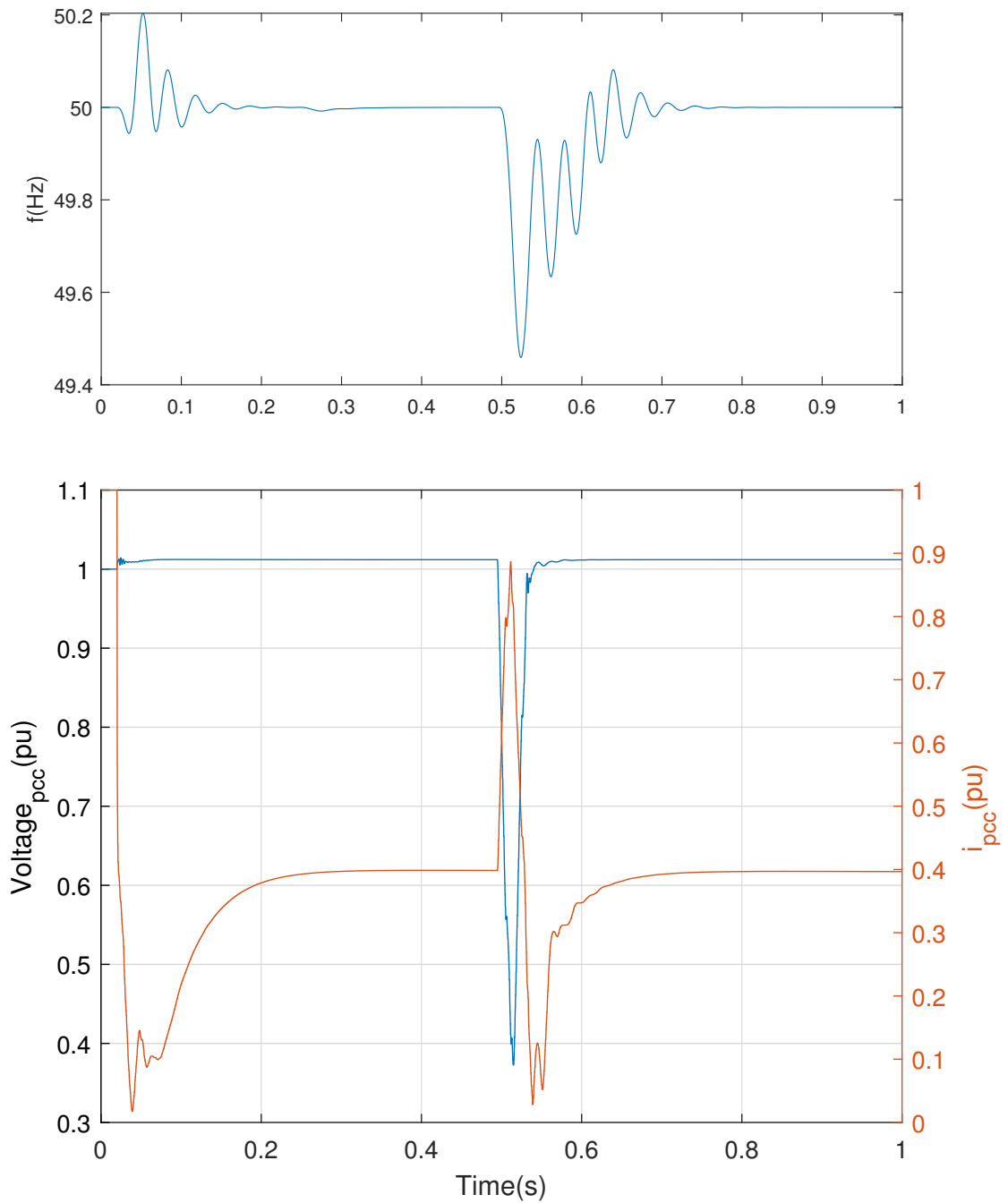


Figure 5-8: Response to a three-phase to ground fault

Test 5: Response to a load-jump: at a certain point of time, a 1 MW load is connected to the network as shown in Figure 5-1. Because of the higher power demand compared to power generation, the frequency of the grid drops as seen in Figure 5-9, but it's recovered within milliseconds by the support of the fast power converter response as well as the infinite grid.

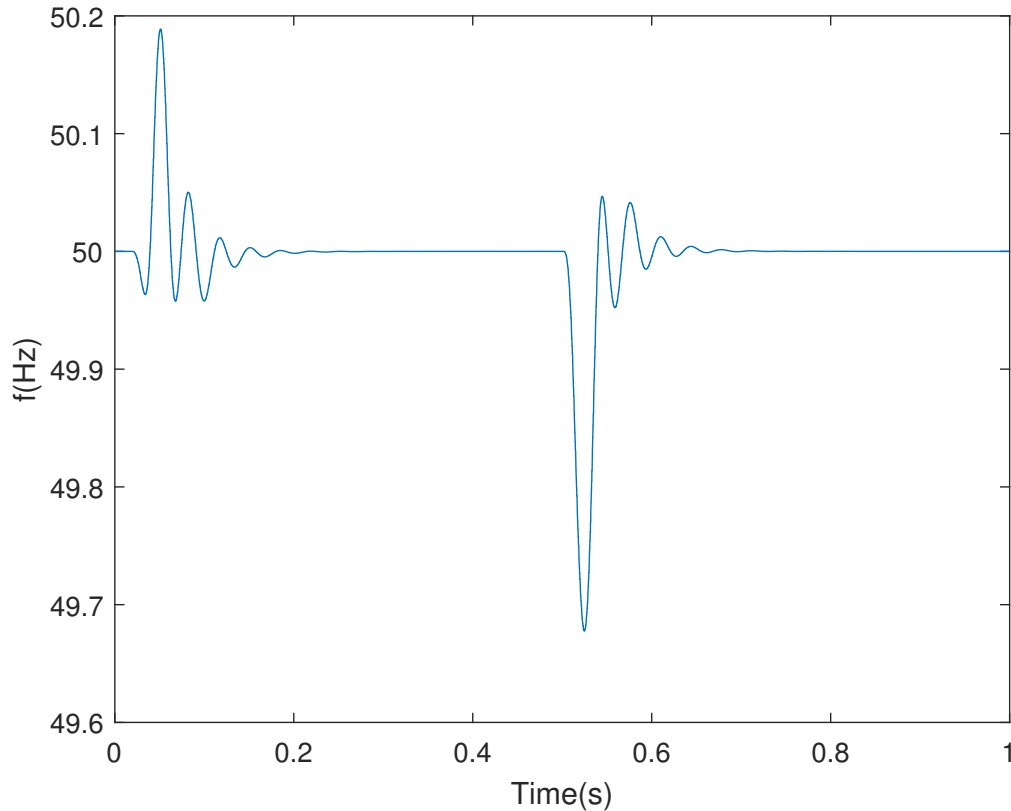


Figure 5-9: Response of the electrolyzer model to a load jump

From the tests of both power system disturbances, it's observable that the PEM electrolyzer model responds within the time range of the inertial response of a synchronous generator. This fast response demonstrates the potential of the stack for frequency compensation of the grid in case of exposure to disturbances.

Chapter 6

Conclusion

This thesis developed a generic electrical model for a grid-connected Proton Exchange Membrane (PEM) electrolyzer that is appropriate for power system stability studies. Moreover, it analyzed how this technology can contribute to the operation of the power system through the procurement of ancillary services.

To investigate the transient properties, the dynamic model of the PEM electrolyzer is developed based on its electrochemical model by neglecting its thermal sub model and Balance of Plant (BoP) components due to a respective high response time and constant power consumption. In addition, the electrolyzer is interfaced to the grid via a series connection of a rectifier, which comprises an inner controller for the line current, and the buck converter with a switch that controls the current flow to the PEM stack.

The electrolyzer's rectifier is modeled with an average mode which performs as a three-phase, two level, Pulse Width Modulation (PWM) converter, except that switching frequency phenomena are averaged over the switching period. The principle is to make a continuous model that averaged over one switching period has the same terminal voltage-current relationship as a full, switched, model. The model makes it possible to run simulations with much larger time step, resulting in simulations, which run faster and therefore larger time spans are possible.

The controllability of the electrolyzer in the millisecond time level is utilized with a high level control to demonstrate grid-supporting capabilities. The proposed high-level control scheme attempts to bridge the gap between the capabilities of the electrolyzer model with low level controls and the requirements of various ancillary services. With such control design, this study demonstrates automated and flexible electrolyzer operation to participate in demand response programs, frequency support and local voltage support with reasonably fast response times. Furthermore, it should be noted that this high level control scheme is open to be done in future work to have the capability to communicate and respond simultaneously to the signals sent, for instance, from market, Transmission System Operators (TSO) and local alarms. To study the impact of the electrolyzer on power system stability, various EMT simulations have been performed using test cases in chapter 5. These continuous-time simulations show that the electrolyzer has a positive effect on frequency stability, as the electrolyzer is able to respond faster to frequency deviations than conventional generator governors, even if the effect of dynamic load of the electrolyzer on the aging rate of the stack need to be studied

as well. Moreover, the electrolyzer can reduce or enhance its electrical consumption with a high range for unlimited amount of time that indicates its potential to act as a secondary or tertiary frequency control. Thus, it can be concluded that electrolyzers can be operated to support a variety of applications, while also providing hydrogen for industrial processes, transportation fuel or heating fuel.

The PEM electrolyzer model implemented in this study has the possibility to be expended to large scale electrolyzer by parallel connection of several small stacks, assuming the response time does not increase significantly with electrolyzer capability, albeit open for further study.

Bibliography

- [1] B. Yodwong, D. Guilbert, M. Phattanasak, W. Kaewmanee, M. Hinaje, and G. Vitale, “AC-DC Converters for Electrolyzer Applications: State of the Art and Future Challenges,” *Electronics*, vol. 9, no. 912, pp. 1–31, 2020.
- [2] P. W. Sauer and M. A. Pai, *Power System Dynamics and Stability*. Upper Saddle River, NJ, USA: Prentice-Hall, 2006.
- [3] P. Kundur, *Power System Stability and Control*. NY, USA: McGraw-Hill, 1994.
- [4] U. Markovic, O. Stanojevic, E. Vrettos, P. Aristidou, and G. Hug, “Understanding Stability of Low-Inertia Systems,” *IEEE Members, International Journal of Computer Applications*, 2019.
- [5] J. J. Caparrós Mancera, F. S. Manzano, J. M. Andújar, F. J. Vivas, and A. J. Calderón, “An Optimized Balance of Plant for a Medium-Size PEM Electrolyzer: Design, Control and Physical Implementation,” *Electronics*, vol. 9, no. 871, pp. 1–25, 2020.
- [6] M. Khatib and S. Ahmed, “Impact of Distributed Energy Resources on Frequency Regulation of the Bulk Power System,” *2019 IEEE Conference on Power Electronics and Renewable Energy (CPERE)*, pp. 258–263, 2019.
- [7] N. Veerakumar, M. E. Adabi, J. R. Torres, P. Gonzalez-Longatt, Z. Ahmad, J. L. R. Torres, A. M. M. Meijden, and P. Palensky, “Fast Active Power-Frequency Support Methods by Large Scale Electrolyzers for Multi-Energy Systems,” *2020 IEEE PES Innovative Smart Grid Technologies Europe (ISGT-Europe)*, pp. 151–155, 2020.
- [8] B. W. Tuinema, E. Adabi, P. K. S. Ayivor, V. G. Suárez, L. Liu, A. Perilla, Z. Ahmad, J. L. R. Torres, A. M. M. Meijden, and P. Palensky, “Modelling of large-sized electrolyzers for real time simulation and study of the possibility of frequency support by electrolyzers,” *IET Generation, Transmission and Distribution*, vol. 14, no. 10, pp. 1985–1992, 2020.
- [9] A. Samani, S. D’Amicis, D. De Kooning, D. Bozalakov, and P. Silva, “Grid balancing with a large-scale electrolyzer providing primary reserve,” *IET Renewable Power Generation*, vol. 14, no. 16, pp. 3070–3078, 2020.

- [10] H. Weber, "The Ancillary Response of Storage Power Plants (SPP) in the Present and Future Electrical Grid," *ETG/GMA-Fachtagung „Netzregelung und Systemführung"*, pp. 110–115, 2019.
- [11] J. L. Monroy-Morales, M. Herna'ndez-A'ngeles, and D. C. R. P. M. O. W. Merida, "Modeling and Control Design of a Vienna Rectifier Based Electrolyzer," *2016 IEEE 7th International Symposium on Power Electronics for Distributed Generation Systems (PEDG)*, pp. 1–8, 2016.
- [12] F. Alshehri, V. G. Suarez, J. L. R. Torres, A. Perilla, and M. A. M. M. Meijden, "Modelling and evaluation of PEM hydrogen technologies for frequency ancillary services in future multi-energy sustainable power systems," *Heliyon*, vol. 5, pp. 1–24, 2019.
- [13] M. Mohanpurkar, Y. Luo, D. Terlip, F. Dias, K. Harrison, J. Eichman, R. Hovsapian, and J. Kurtz, "Electrolyzers Enhancing Flexibility in Electric Grids," *energies*, vol. 10, no. 1836, pp. 1–17, 2017.
- [14] H. Saadat, *Power System Analysis*. WCB/McGraw-Hill., 1999.
- [15] R. Garcia-Hernandez and R. Garduno-Ramirez, "Modeling a Wind Turbine Synchronous Generator," *International Journal of Energy and Power(IJEP)*, vol. 2, pp. 64–70, 2013.
- [16] A. Tayyebi, D. Groß, A. Anta, F. Kupzog, and F. Dörfler, "Frequency Stability of Synchronous Machines and Grid-Forming Power Converters," *IEEE Explore*, vol. 8, no. 2, pp. 1004–1018, 2020.
- [17] Z. Chen, F. Blaabjerg, and F. Iov, "A study of synchronous machine model implementations in Matlab/Simulink simulations for new and renewable energy systems," *IEEE, International Conference on Electrical Machines and Systems (ICEMS)*, vol. 3, pp. 1960–1965, 2006.
- [18] R. H. Park, "Two-reaction Theory of Synchronous Machines: Generalized Method of Analysis-Part 1," *Transactions of the AIEE*, vol. 48, no. 493, pp. 716–731, 2012.
- [19] S. Leng, *Coordination of multiple active front end converters for power quality improvement*. PhD thesis, Florida State University, Florida, USA, Marth 2012.
- [20] F. Speckmann, S. Bintz, and K. Birke, "Influence of rectifiers on the energy demand and gas quality of alkaline electrolysis systems in dynamic operation," *Applied Energy*, vol. 250, pp. 855–863, 2019.
- [21] B. Yodwong, D. Guilbert, M. Phattanasak, W. Kaewmanee, M. Hinaje, and G. Vitale, "Proton Exchange Membrane Electrolyzer Modeling for Power Electronics Control: A Short Review," *Journal of Carbon Research*, vol. 6, no. 29, pp. 1–20, 2020.
- [22] J. Solanki, P. Wallmeier, J. Böcker, and A. A. N. Fröhleke, "High-current variable-voltage rectifiers: State-of-the-art topologies," *IET Power Electronics*, vol. 8, pp. 1068–1080, 2015.
- [23] B. Yodwong, D. Guilbert, M. Phattanasak, W. Kaewmanee, and M. Phattanasak, "Energy Efficiency Based Control Strategy of a Three-Level Interleaved DC-DC Buck Converter Supplying a Proton Exchange Membrane Electrolyzer," *Electronics*, vol. 8, no. 933, pp. 1–19, 2019.

-
- [24] J. S. H. Z. Ji, L. J. Wei, and X. M. Zha, "A Nonlinear Large-Signal Model for DC-DC Converters," *2016 IEEE 8th International Power Electronics and Motion Control Conference (IPEMC-ECCE Asia)*, p. 2183–2186, 2016.
- [25] F. Gao, D. Blunier, M. G. Simões, and A. Miraoui, "PEM Fuel Cell Stack Modeling for Real-Time Emulation in Hardware-in-the-Loop Applications," *IEEE TRANSACTIONS ON ENERGY CONVERSION*, vol. 26, no. 1, pp. 184–194, 2011.
- [26] D. Guilbert, S. M. Collura, and A. Scipioni, "DC/DC converter topologies for electrolyzers: State-of-the-art and remaining key issues," *ScienceDirect*, vol. 42, no. 38, pp. 23966–23985, 2017.
- [27] V. Guida, D. Guilbert, and B. Douine, "Literature Survey of Interleaved DC-DC Step-Down Converters for Proton Exchange Membrane Electrolyzer Applications," *TRANSACTIONS ON ENVIRONMENT AND ELECTRICAL ENGINEERING*, vol. 3, no. 1, pp. 1–11, 2019.
- [28] IRENA, "Hydrogen from renewable power: Technology outlook for the energy transition," *International Renewable Energy Agency*, 2020.
- [29] H. P. C. Buitendach, R. Gouws, C. A. Martinson, C. Minnaar, and D. Bessarabov, "Effect of a ripple current on the efficiency of a PEM electrolyser," *Results in Engineering*, vol. 10, pp. 1–13, 2021.
- [30] M. Carmo, D. L. Fritz, J. Mergel, and D. Stolten, "A comprehensive review on PEM water electrolysis," *INTERNATIONAL JOURNAL OF HYDROGEN ENERGY*, vol. 38, pp. 4901–4934, 2013.
- [31] A. Buttler and H. Spliethoff, "Current status of water electrolysis for energy storage, grid balancing and sector coupling via power-to-gas and power-to-liquids: A review," *Renewable and Sustainable Energy Reviews*, vol. 10, pp. 1–15, 2017.
- [32] N. Du, R. Peach, and M. T. S. T. Bock, "Anion-Exchange Membrane Water Electrolyzers," *Chemical Reviews Article ASAP*, pp. 1–66, 2022.
- [33] I. Vincent, A. Kruger, D. Bessarabov, C. Minnaar, and D. Bessarabov, "Hydrogen Production by water Electrolysis with an Ultrathin Anion-exchange membrane (AEM)," *International Journal of ELECTROCHEMICAL SCIENCE*, vol. 13, pp. 11347–11358, 2018.
- [34] A. Ursua, L. M. Gandia, and P. Sanchis, "Hydrogen Production From Water Electrolysis: Current Status and Future Trends," in *Proceedings of the IEEE*, vol. 100, no. 2, pp. 410–426, 2012.
- [35] O. Ulleberg, "Modeling of advanced alkaline electrolyzers: a system simulation approach," *International Journal of Hydrogen Energy*, vol. 28, no. 1, pp. 21–33, 2003.
- [36] M. Lebbal and S. Lecoeuche, "Identification and monitoring of a PEM electrolyser based on dynamical modelling," *INTERNATIONAL JOURNAL OF HYDROGEN ENERGY*, vol. 34, p. 5992–5999, 2009.

- [37] C. Martinson, G. van Schoor, K. Uren, and D. Bessarabov, "Proton exchange membrane electrolyzer based on current interruption," *2013 IEEE International conference on Industrial Technology (ICIT)*, pp. 716–721, 2013.
- [38] A. Ursu 'a and P. Sanchis, "Static-dynamic modeling of the electrical behavior of a commercial advanced alkaline water electrolyzer," *International Journal of Hydrogen Energy*, vol. 37, no. 2, pp. 18598–18614, 2012.
- [39] M. Espinosa-Lopez, C. Darras, P. Poggi, R. , P. Baucour, S. Rakotondrainibe, A. Besse, and P.Serre-Combe, "Modelling and experimental validation of a 46 kW PEM high pressure water electrolyzer," *Renewable Energy*, vol. 119, pp. 160–173, 2018.
- [40] B. Yodwong, D. Guilbert, M. Phattanasak, W. Kaewmanee, M. Hinaje, and G. Vitale, "Faraday's efficiency Modeling of a Proton Exchange Membrane Electrolyzer Based on Experimental Data," *Energies*, vol. 13, no. 18, pp. 1–14, 2020.
- [41] H. Vogelesang, "An introduction to energy consumption in pumps," *World Pumps*, vol. 8, no. 493, pp. 28–31, 2008.
- [42] A. Arif, Z. Wang, J. Wang, B. Mather, and H. Bashualdo, "Load Modeling—A Review," *IEEE TRANSACTIONS ON SMART GRID*, vol. 9, no. 6, pp. 5986–5999, 2018.
- [43] Y. Lin, B. Johnson, V. Gevorgian, V. Purba, and S. Dhople, "Stability assessment of a system comprising a single machine and inverter with scalable ratings," *EEE Xplore, North American Power Symposium (NAPS)*, 2017.
- [44] S. Tesnjak, G. Erceg, R. Erceg, and D. K. Z. Komericki, "Excitation System of Synchronous Turbo Generator," *Thermal Power Plant Features in the Meaning of Electric Power System Demands,HEP*, 2000.
- [45] J. Machowski, W. Bialek, S. Robak, and R. Bumby, "Excitation control system for use with synchronous generators," *IEE Proc. Gener. Transm. Distrib.*, vol. 145, 1998.
- [46] J. Vedrana, M. Kresimir, and S. Zeljko, "Excitation System Models of Synchronous Generator," *28th International Conference Science*, 2018.
- [47] O. Rolf, *On Control of Back-to-Back Converters and Sensorless Induction Machine Drives*. PhD thesis, Chalmers University of Technology, Göteborg, Sweden, 2003.
- [48] M. Yazdanian and A. Mehrizi-Sani, "Internal Model-Based Current Control of the RL Filter-Based Voltage-Sourced Converter," *IEEE TRANSACTIONS ON ENERGY CONVERSION*, vol. 29, no. 4, pp. 873–881, 2014.
- [49] P. Ayivor, P. Torres, and M. Meijden, "Modelling of Large Size Electrolyzer for Electrical Grid Stability Studies in Real Time Digital Simulation," *Proc. 17th Wind Integration Workshop October 2018*, 2018.
- [50] G. Misyris, J. Mermet-Guyennet, S. Chatzivasileiadis, and T. Weckesser, "Grid Supporting VSCs in Power Systems with Varying Inertia and Short-Circuit Capacity," *2019 IEEE Milan PowerTech*, pp. 1–6, 2019.

-
- [51] A. Yazdani and R. Iravani, *VOLTAGE-SOURCED CONVERTERS IN POWER SYSTEMS*. John Wiley and Sons, Inc., 2010.
- [52] D. Rabie, Y. S. Mohamed, and E. G. Shehata, "Voltage Source Converter Control and Stability Analysis of VSC-HVDC System with High DC-Link Impedance," *2019 21st International Middle East Power Systems Conference (MEPCON)*, pp. 667–674, 2019.
- [53] M. Mendalek and K. Al-Haddad, "Modeling and nonlinear control of shunt active power filter in the synchronous reference frame," *Proc. (Cat. No.00EX441) Ninth Int Conf. Harmonics and Quality of Power*, vol. 1, no. 1, pp. 30–35, 2000.
- [54] P. Olivier, C. Bourasseau, and P. B. Bouamama, "Low-temperature electrolysis system modelling: A review," *Renewable and Sustainable Energy Reviews*, vol. 78, pp. 280–300, 2017.
- [55] G. Lichtenberg, G. Pangalos, C. C. Yáñez, A. Luax, N. Jöres, L. Schnelle, and C. Kaufmann, "Implicit multilinear modeling," *DE GRUYTER OLDENBOURG*, vol. 1, no. 70, pp. 13–30, 2022.
- [56] F. Milano, F. Dörfler, G. Hug, D. J. Hill, and G. Verbič, "Foundations and Challenges of Low-Inertia Systems," *2018 Power Systems Computation Conference (PSCC)*, pp. 1–25, 2018.
- [57] M. G. Dozein, A. Jalali, and P. Mancarella, "Fast Frequency Response From Utility-Scale Hydrogen Electrolyzers," *IEEE TRANSACTIONS ON SUSTAINABLE ENERGY*, vol. 12, no. 3, pp. 1707–1717, 2021.
- [58] N. Chiesa, Y. Korpås, E. Kongstein, and A. Ødegaard, "Dynamic control of an electrolyser for voltage quality enhancement," *International Conference on Power Systems Transients (IPST)*, pp. 1–7, 2011.
- [59] M. G. Dozein, A. Jalali, and P. Mancarella, "Novel Electrolyzer Applications: Providing More Than Just Hydrogen," *National Renewable Energy Laboratory (NREL)*, available at www.nrel.gov/publications, 2014.
- [60] J. J. Grainger and W. D. Stevenson, *Power System Analysis*. McGraw-Hill New York, 1994.

Glossary

List of Acronyms

PEM	Proton Exchange Membrane
ESS	Energy Storage Systems
VSC	Voltage Source Converter
AFE	Active Front End
EMF	Electromotive Force
TSO	Transmission System Operators
BoP	Balance of Plant
PI	Proportional Integral
SM	Synchronous Machine
LTI	Linear Time-invariant System
AVR	Automatic Voltage Regulator
PSS	Power System Stabilizer
IMC	Internal Model Control
PLL	Phase-Locked Loop
PWM	Pulse Width Modulation
IGBT	Integrated Gate Bipolar Transistors
SPWM	Sinusoidal Pulse Width Modulation
CCM	Continuous Conduction Mode
IRENA	International Renewable Energy Agency
CAPEX	capital expenditure
OPEX	operating expense
AEM	Anion Exchange Membrane
SOE	Solid Oxide Electrolyzer

KOH	potassium hydroxide
redox	reduction oxidation
PC	polarization curve
EIS	electrochemical impedance spectroscopy
OCV	Open Circuit Voltage
BoP	Balance of Plant
HPS	High Pressure Separator
LPS	Low Pressure Separator
PSA	Pressure Swing Adsorption
PMU	Phasor Measurement Unit
RoCoF	rate of change of frequency
aFRR	Automatic Frequency Restoration Reserve
FCR	Frequency Containment Reserve
FAPR	Fast Active Power Regulator
EMT	Electromagnetic Transient
STATCOM	static synchronous compensator
PCC	Point of Common Coupling

List of Symbols

α	Bandwidth of a controller
η	Efficiency
θ	Phase angle
ω	Angular velocity
ψ	Flux linkage
C	Capacitor
f	Frequency
i	Current
J	Inertia constant
L	Inductance
n	Synchronous speed
P	Active power
p	Pole pairs
Q	Reactive power
R	Resistance
R	Universal gas constant

S	Apparent power
T	Temperature
T_e	Electrical torque
T_m	Mechanical torque
V	Voltage
z	Valency electrons

An Appendix

-1 Electrolyzer model

In this section, the key parameters of the PEM electrolyzer used in the model are listed in a table.

Table 1: Parameters of the PEM electrolyzer model

Parameter name	Symbol	Value
Cell active surface	A	290 cm ²
Series connected cells	N_c	60
Temperature	T	60 °C
Anode pressure	P_{O_2}	34 bar
Cathode pressure	P_{H_2}	35 bar
Power consumption	P_{ely}	46 kW
Charge transfer coefficient	α_a	0.7353
exchange current density	$i_{0,a-std}$	1.08e - 8 A/cm ²
specific cell capacity	$C_{DL,cell}$	38 * 10 ⁻⁴ F/cm ²
Membrane thickness	δ_{mem}	0.0178 cm
Protonic conductivity	$\sigma_{mem,std}$	0.1031 S/cm
Activation energy	E_{pro}	10536 Jmol ⁻¹

-2 A MATLAB listing

This section contains a MATLAB function to solve the nonlinearity of the PEM electrolyzer due to the RC element of the equivalent electric circuit.

```

1 function [dVact] = fcn(I,Vact)
2 %
3 %% Activation overpotential
4 F=96485; % Faraday constant [C/mol]
5 R=8.314; % universal gas constant [J.K-1. mol-1]
6 T=273.15+60; % Operating temperature
7 Tstd=273.15+25; % temp at a standard condition
8 A=290; % cell area in cm^2
9 i=I/A; % Current density [A cm-2]
10 aan=0.7353; % charge transfer coefficient
11 ioan_std=1.08e-8; % exchange current density for Pt-Ir anode catalyst
12 Eexc=52994; % activation energy
13 Nc=60; % number of series connected cells
14 ioan=ioan_std*exp(-(Eexc/R)*(1/T-1/Tstd)); % Arrhenius expression
15 Vacti=(R*T)/(2*aan*F)*asinh((i)/(2*ioan)); % Volmer-Butler-Equation for
    one cell
16 Ract=Vacti/I*Nc;
17 %% Double-layer Capacitor
18 Cd=1.38*10^-4; % [F cm-2]
19 Cd1=(Cd*A)/Nc;
20 dVact=Cd1^-1*I-(1/(Cd1*Ract)*Vact);

```

-3 Controller parameters

The parameters of all proportional (kp) and integral (ki) controllers are stated in this section.

```

1 %% Converter parameters
2 S_Tr=500e3; % Nominal power of step-down transformer
3 V2_rms=240; % Secondary winding voltage of transformer
4 Vdc_n=sqrt(6)*V2_rms; % Out voltage of the rectifier
5 R_f=0.1e-3;L_f=20e-6; % line filter parameters
6 C_dc=0.00375; % DC-link Capacitance
7 % Inner current control parameters
8 wL_f=0.1055; % product of angular velocity and inductance of trasmission
    line in pu
9 kpv=20.09;kiv=4185.417; % outer voltage controller
10 kip=0.6628;kii=14.622; % inner current controller
11 %% Higher level controllers
12 % Power control
13 Pref=0.75; % reference power of electrolyzer in pu
14 k_d=20; % droop coefficient
15 kpp=1e-6;kpi=0.001;
16 % voltage control
17 Vref=1; % reference voltage of AC grid in pu
18 kvp=0.5;kvi=0;

```